Inorg. Chem. **2003**, *42*, 6824–6850

Investigation of the Reduced High-Potential Iron–Sulfur Protein from *Chromatium vinosum* and Relevant Model Compounds: A Unified Picture of the Electronic Structure of $[Fe_4S_4]^{2+}$ Systems through Magnetic and Optical Studies

Latévi M. Lawson Daku,*,† Jacques Pécaut, Alix Lenormand-Foucaut, Béatrice Vieux-Melchior, Peter Iveson, and Jeanne Jordanov

Service de Chimie Inorganique et Biologique, UMR 5046, Département de Recherche Fondamentale sur la Matière Condensée, CEA-Grenoble, 17 rue des Martyrs, 38054 Grenoble Cedex 9, France

Received May 10, 2003

Magnetization measurements and variable temperature optical spectroscopy have been used to investigate, within the 4–300 K temperature range, the electronic structure of the reduced high-potential iron protein (HiPIP) from *Chromatium vinosum* and the model compounds $(Cat)_2[Fe_4S_4(SR)_4]$, where RS^- = 2,4,6-triisopropylphenylthiolate (**1**), 2,6-diphenylphenylthiolate (**2**), diphenylmethylthiolate (**3**), 2,4,6-triisopropylbenzylthiolate (**4**, **4′**), 2,4,6-triphenylbenzylthiolate (**5**, **5′**), 2,4,6-tri-*tert*-butylbenzylthiolate (**6**), and $Cat^+ = {}^+NEt_4$ (**1**, **2**, **3**, **4′**, **5′**, **6**), ${}^+PPh_4$ (**4**, **5**). The newly synthesized $\mathbf{2}^{2-}$, $\mathbf{3}^{2-}$, $\mathbf{5}^{2-}$, and $\mathbf{6}^{2-}$ complexes are, as $\mathbf{1}^{2-}$ and $\mathbf{4}^{2-}$, excellent models of the reduced HiPIPs: they exhibit the $[Fe_4S_4]^{3+/2+}$ redox couple, because of the presence of bulky ligands which stabilize the $[Fe_4S_4]^{3+}$ oxidized core. Moreover, the presence of SCH_2 groups in $\mathbf{4}^{2-}$, $\mathbf{5}^{2-}$, and $\mathbf{6}^{2-}$, as in the $[Fe_4S_4]$ protein cores, makes them good biomimetic models of the HiPIPs. The X-ray structure of **2** is reported: it crystallizes in the orthorhombic space group *Pcca* with no imposed symmetry and a D_{2d}-distorted geometry of the $[Fe_4S_4]^{2+}$ core. Fit of the magnetization data of the reduced HiPIP and of the **1**, **2**, **3**, **4**, **5**, and **6** compounds within the exchange and double exchange theoretical framework leads to exchange coupling parameters $J = 261–397$ cm^{-1}. A firm determination of the double exchange parameters B or, equivalently, the transfer integrals $\beta = 5B$ could not be achieved that way. The obtained $|B|$ values remain however high, attesting thus to the strength of the spin-dependent electronic delocalization which is responsible for lowest lying electronic states being characterized by delocalized mixed-valence pairs of maximum spin $^9/_2$. Electronic properties of these systems are then accounted for by the population of a diamagnetic ground level and excited paramagnetic triplet and quintet levels, which are respectively J and $3J$ above the ground level. Optical studies of **1**, **2**, **4′**, **5′**, and **6** but also of $(NEt_4)_2[Fe_4S_4(SCH_2C_6H_5)_4]$ and the isomorph $(NEt_4)_2[Fe_4S_4(S\text{-}t\text{-}Bu)_4]$ and $(NEt_4)_2[Fe_4Se_4(S\text{-}t\text{-}Bu)_4]$ compounds reveal two absorption bands in the near infrared region, at 705–760 nm and 1270–1430 nm, which appear to be characteristic of valence-delocalized and ferromagnetically coupled $[Fe_2X_2]^+$ (X = S, Se) units. The $|B|$ and $|\beta|$ values can be directly determined from the location at $10|B|$ of the low-energy band, and are respectively of 699–787 and 3497–3937 cm^{-1}. Both absorption bands are also present in the 77 K spectrum of the reduced HiPIP, at 700 and 1040 nm (Cerdonio, M.; Wang, R.-H.; Rawlings, J.; Gray, H. B. *J. Am. Chem. Soc.* **1974**, *96,* 6534–6535). The blue shift of the low-energy band is attributed to the inequivalent environments of the Fe sites in the protein, rather than to an increase of $|\beta|$ when going from the models to the HiPIP. The small differences observed in known geometries of $[Fe_4S_4]^{2+}$ clusters, especially in the Fe–Fe distances, cannot probably lead to drastic changes in the direct Fe–Fe interactions (parameter β) responsible for the delocalization phenomenon. These differences are however magnetostructurally significant as shown by the 261–397 cm^{-1} range spanned by J. The cluster's geometry, hence the efficiency of the Fe–μ_3-S–Fe superexchange pathways, is proposed to be controlled by the more or less tight fit of the cluster within the cavity provided by its environment.

Introduction

High-potential iron−sulfur proteins (HiPIPs)[1] are small (ca. 60−85 amino acids) metalloproteins possessing the cubane-like $[Fe_4S_4]$ cluster as prosthetic group. Such clusters are present at the active site of a large number of enzymes and electron-transfer proteins, under three different redox

* Corresponding author. E-mail: max.lawson@chiphy.unige.ch.

† Present address: Laboratoire de photophysique et photochimie de composés de métaux de transitions, Département de Chimie Physique, Université de Genève, 30 quai Ernest-Ansermet, 1211 Genève 4, Switzerland.

(1) Abbreviations used: ENDOR, electron nuclear double resonance; EPR, electronic paramagnetic resonance; Fd, ferredoxin; HiPIP, high-potential iron−sulfur protein; His, histidine; MCD, magnetic circular dichroism; NHE, normal hydrogen electrode; NIR, near infrared; NMR, nuclear magnetic resonance; Phe, phenylalanine; RR, resonance Raman; SCE, saturated calomel electrode; SQUID, superconducting quantum interference device; TIC, temperature independent correction; Trp, tryptophane; Tyr, tyrosine; VTMCD, variable temperature magnetic circular dichroism; XAS, X-ray absorption spectroscopy.

10.1021/ic034494n CCC: $25.00
Published on Web 09/24/2003

states: $[Fe_4S_4]^{+}$, $[Fe_4S_4]^{2+}$, $[Fe_4S_4]^{3+}$.[2−4] The first two oxidation states are found in ferredoxins (Fds) which can thus exchange electrons at low potential, in the −650 to −250 mV range vs NHE. The latter two redox states are found in HiPIPs whose designation originates from the higher values taken by the potential of the $[Fe_4S_4]^{3+}/[Fe_4S_4]^{2+}$ couple, in the +50 to +400 mV range vs NHE. HiPIPs are isolated from phototropic bacteria, and may act as electron transfer-only agents.[5] The relationship between the structure of an $[Fe_4S_4]$ protein and its redox properties has been extensively discussed;[6−13] the existence and stability of the highest oxidation level $[Fe_4S_4]^{3+}$ have been directly ascribed to the location of the cluster in a hydrophobic pocket which limits the solvent accessibility. In most chemical models, the $[Fe_4S_4]^{2+/3+}$ redox process remains either undetected or irreversible. Use of the aromatic bulky 2,4,6-trimethylphenylthiolate and 2,4,6-triisopropylphenylthiolate ligands resulted in the first observation of the reversible $[Fe_4S_4]^{2+/3+}$ redox process.[14] Soon thereafter, the synthesis and crystallographic characterization of the oxidized species $[Fe_4S_4(S\text{-}2,4,6\text{-}(i\text{-}Pr)_3C_6H_2)_4]^{-}$ was reported.[15] These results indicated that it was possible to design chemical models with ligands able to stabilize the $[Fe_4S_4]$ cluster in its higher oxidation state. The existence of the $[Fe_4S_4]^{3+}$ core, albeit only stable at the cyclic voltammetry time scale, was observed in solution with thiolates such as adamantanethiolate.[16,17] Recently, we reported the synthesis of a new $[Fe_4S_4]$ cluster with a ligand presenting a SCH_2 group as in cysteine, namely, the more biomimetic bulky 2,4,6-triisopropylbenzylthiolate ligand.[18] The $[Fe_4S_4]^{3+}$ core was found to be relatively well stabilized in solution, and the system could be studied by ^{1}H NMR in the $[Fe_4S_4]^{3+/2+}$ oxidation states. We have now synthesized new $[Fe_4S_4]$ clusters with ligands belonging to three different groups.[19,20] With the 2,6-diphenylphenylthiolate ligand we have added a new member to the phenylthiolate group; the biomimetic bulky benzylthiolate group has been augmented with the 2,4,6-triphenylbenzylthiolate and 2,4,6-tri-*tert*-butylbenzylthiolate ligands. These ligands have allowed the isolation in the solid state of the oxidized species $[Fe_4S_4(S\text{-}2,6\text{-}(Ph)_2C_6H_3)_4]^{-}$, $[Fe_4S_4(SCH_2\text{-}2,4,6\text{-}(Ph)_3C_6H_2)_4]^{-}$, and $[Fe_4S_4(SCH_2\text{-}2,4,6\text{-}(t\text{-}Bu)_3C_6H_2)_4]^{-}$.[19,20] The diphenylmethylthiolate ligand defines the third group. In our strategy to obtain new HiPIP models, this ligand with a thiol function carried by an sp^3 carbon atom provides an intermediate situation between those of the phenylthiolate and the benzylthiolate ligands. These new analogues allowed us to probe the influence of the cluster's environment on the electronic structure of the $[Fe_4S_4]^{3+/2+}$ cores.

Reported studies of the electronic structure of $[Fe_4S_4]$ clusters remain essentially based on the analysis of data obtained by use of spectroscopic techniques. Thus, EPR, ENDOR, MCD, and Mössbauer spectroscopies provide fine structural information on paramagnetic species. However, because of the very fast relaxation of the electronic spin (10^{-13}−10^{-8} s), the domain of investigation of the above-mentioned spectroscopies is limited to cryogenic temperatures, where the mainly populated state is the ground state. As for $[Fe_4S_4]^{2+}$ systems, the diamagnetic ground state of several such model complexes was recently characterized by S K-edge X-ray absorption spectroscopy.[21] Conversely NMR spectroscopy operates at high temperatures (∼300 K) where excited states became thermally populated. Consequently, the fine structural information obtained by NMR spectroscopy characterizes simultaneously all the thermally populated electronic states of the studied systems. It is obvious that a reliable description of the thermally accessible electronic states of Fe−S systems should also rely on the analysis of data recorded over a larger temperature range than those available individually to the techniques mentioned above. As Fe−S systems possess thermally accessible paramagnetic states, this condition can be fulfilled by performing magnetization studies, as modern magnetometers allow the acquisition of data over an important temperature range. We have therefore articulated our studies around the analysis of magnetization data recorded over the 4−300 K temperature range. In our ongoing effort to understand HiPIP chemical and physical properties, we have studied several models in the $[Fe_4S_4]^{3+/2+}$ redox states, as well as the HiPIP

(2) Spiro, T. G., Ed. *Iron-Sulfur Proteins;* Wiley-Interscience: New York, 1982.
(3) Johnson, M. K. In *Encyclopedia of Inorganic Chemistry*; King, R. B., Ed.; Wiley: New York, 1994.
(4) Beinert, H.; Holm, R. H.; Münck, E. *Science* **1997**, *277*, 653−659 and references therein.
(5) Tedro, S. M.; Meyer, T. E.; Kamen, M. D. *Arch. Biochem. Biophys.* **1985**, *241*, 656−664.
(6) Carter, C. W., Jr.; Kraut, J.; Freer, S. T.; Xuong, N.-H.; Alden, R. A.; Bartsch, R. G. *J. Biol. Chem.* **1974**, *249*, 4212−4225.
(7) Adman, E. T.; Watenpaugh, K. D.; Jensen, L. H. *Proc. Natl. Acad. Sci. U.S.A.* **1975**, *72*, 4854−4858.
(8) Carter, C. W., Jr. *J. Biol. Chem.* **1977**, *252*, 7802−7811.
(9) Sheridan, R. P.; Allen, L. C.; Carter, C. W., Jr. *J. Biol. Chem.* **1981**, *256*, 5052−5057.
(10) Czernuszewicz, R. S.; Macor, K. A.; Johnson, M. K. Gewirth, A.; Spiro, T. G. *J. Am. Chem. Soc.* **1987**, *109*, 7178−7187.
(11) Backes, G.; Mino, Y.; Loehr, T. M.; Meyer, T. E.; Cusanovich, M. A.; Sweeney, W. V.; Adman, E. T.; J., S.-L. *J. Am. Chem. Soc.* **1991**, *113*, 2055−2064.
(12) Agarwal, A.; Li, D.; Cowan, J. A. *Proc. Natl. Acad. Sci. U.S.A.* **1995**, *92*, 9440−9444.
(13) Stephens, P. J.; Jollie, D. R.; Warshel, A. *Chem. Rev.* **1996**, *96*, 2491−2513.
(14) Ueyama, N.; Terakawa, T.; Sugawara, T.; Fuji, M.; Nakamura, N. *Chem. Lett.* **1984**, 1287−1290.
(15) O'Sullivan, T.; Millar, M. M. *J. Am. Chem. Soc.* **1985**, *107*, 4096−4097.
(16) Okuno, Y.; Uoto, K.; Yonemitsu, O.; Tomohiro, T. *J. Chem. Soc., Chem. Commun.* **1987**, 1018−1020.
(17) Kambayashi, H.; Nagao, H.; Tanaka, K.; Nakamoto, M.; S., P. *Inorg. Chim. Acta* **1993**, *209*, 143−149.
(18) Lenormand, A.; Iveson, P.; Jordanov, J. *Inorg. Chim. Acta* **1996**, *251*, 119−123.
(19) Lenormand-Foucaut, A. Modélisation chimique de protéines fer-soufre à haut potentiel: synthèses et caractérisations physico-chimiques de nouveaux agrégats à ligands thiolates encombrés dans les états $[4Fe\text{-}4S]^{2+}$ et $[4Fe\text{-}4S]^{3+}$. Thesis, Université Joseph Fourier, 1996.
(20) Vieux-Melchior, B. Un nouveau modèle de protéine fer-soufre à haut potentiel, à ligands thiolates encombrés et dans les états $[4Fe\text{-}4S]^{2+}$ et $[4Fe\text{-}4S]^{3+}$: synthèse et caractérisations physico-chimiques. Master's Thesis, Université Joseph Fourier, 1996.
(21) Glaser, T.; Rose, K.; Shadle, S. E.; Hedman, B.; Hodgson, K. O.; Solomon, E. I. *J. Am. Chem. Soc.* **2001**, *123*, 442−454 and references therein.

from *Chromatium vinosum* in both oxidation states.[19,20,22] In this paper, we relate the results obtained for the reduced HiPIP and the reduced model compounds $(NEt_4)_2[Fe_4S_4(S\text{-}2,4,6\text{-}(i\text{-}Pr)_3C_6H_2)_4]$ (**1**), $(NEt_4)_2[Fe_4S_4(S\text{-}2,6\text{-}(Ph)_2C_6H_3)_4]$ (**2**), $(NEt_4)_2[Fe_4S_4(SCH(Ph)_2)_4]$ (**3**), $(PPh_4)_2[Fe_4S_4(SCH_2\text{-}2,4,6\text{-}(i\text{-}Pr)_3C_6H_3)_4]$ (**4**), $(NEt_4)_2[Fe_4S_4(SCH_2\text{-}2,4,6\text{-}(i\text{-}Pr)_3C_6H_3)_4]$ (**4′**), $(PPh_4)_2[Fe_4S_4(SCH_2\text{-}2,4,6\text{-}(Ph)_3C_6H_2)_4]$ (**5**), $(NEt_4)_2[Fe_4S_4(SCH_2\text{-}2,4,6\text{-}(Ph)_3C_6H_2)_4]$ (**5′**), and $(NEt_4)_2[Fe_4S_4(SCH_2\text{-}2,4,6\text{-}(t\text{-}Bu)_3C_6H_2)_4]$ (**6**). The crystal structure of the novel $[Fe_4S_4(S\text{-}2,6\text{-}(Ph)_2C_6H_3)_4]^{2-}$ dianion has been solved for identification purposes. Analysis of the magnetization data was performed in the theoretical framework of exchange and double exchange interactions and thus differs from the previously reported magnetization studies of $[Fe_4S_4]^{2+}$ clusters (which used a pure exchange approach to fit the data),[23−25] by appropriately accounting for the spin dependent electronic delocalization phenomenon occurring in such clusters. It has resulted in a relatively simple model for the electronic structure of the models and of HiPIP. Using variable temperature optical measurements over the 10−300 K temperature range, we have identified in the near infrared (NIR) domain electronic transitions associated with the electronic delocalization in these mixed-valence compounds. The combined results of magnetic and optical studies allow us to give a clear and unified picture of the electronic structure of these $[Fe_4S_4]^{2+}$ systems.

Experimental Section

All manipulations of the model compounds and of the HiPIP were carried out under anaerobic conditions (argon, helium, nitrogen), using Schlenk techniques or a Jacomex glovebox. Acetonitrile, dichloromethane, ethanol, methanol, and diethyl ether were distilled under argon over drying agents (CaH_2 for CH_3CN, C_2H_5OH, and CH_2Cl_2, $CaCl_2$ for CH_3OH, Na/benzophenone for diethyl ether). Nitrobenzene was distilled under argon and at reduced pressure. Distilled H_2O and D_2O, hexane, and toluene were degassed. Elemental analyses were performed by the Service Central d'Analyze (Vernaison, France) for the ligands, and by the Analytischen Laboratorien (Lindlar, Germany) for the model compounds. ^1H NMR spectra of the ligands were run in CD_2Cl_2 and on a Brucker AC 200 spectrometer. The NMR experiments on the model compounds (^1H spectra, T_1 determination, chemical shift temperature dependence) were carried out on a Varian Unity 400 spectrometer. The model compounds were dissolved in CD_3CN or CD_2Cl_2 and located in hermetically sealed Young tubes; their rotation was obtained by use of a nitrogen gas flow. The solvent residual peak was used as internal reference.

Ligand Synthesis. 2,4,6-Triisopropylphenylthiol was prepared according to a literature procedure.[15]

2,6-Diphenylphenylthiol was also prepared according to a published method.[26] However, the last three steps were adapted to optimize the yield. Synthesis of $2,6\text{-}(C_6H_5)_2C_6H_3OC(S)N(CH_3)_2$: NaH (160 mmol, 3.9 g) is added to a solution of 2,6-diphenylphenol (150 mmol, 37 g) in DMF (200 mL). The reaction mixture is vigorously stirred. When no more gaseous evolution is observed, *N*,*N*-dimethylthiocarbamoyl chloride is added (150 mmol, 15 g), and the mixture is heated to 100 °C for 2 h and then let back to room temperature. The reaction mixture is poured into an aqueous 2% KOH solution (500 mL). The precipitate is filtered and recrystallized from hot ethanol (17 g, 34% yield). Isomerization step: 16.2 g of $2,6\text{-}(C_6H_5)_2C_6H_3OC(S)N(CH_3)_2$ is dissolved in diphenyl ether (450 mL) and heated at 250 °C under argon for 21 h. Most of the solvent is then eliminated by vacuum distillation, and the residual oil solidifies. The solid is dissolved in 5 mL of CH_2Cl_2 and run over a silica gel 60 column, to eliminate the residual diphenyl ether. The final product is recrystallized from hot methanol (12.9 g, 65% yield). ^1H NMR: δ 2.7 (6H, s, CH3); 7.3−7.6 (13H, m, phenyl). Deprotection step: $2,6\text{-}(C_6H_5)_2C_6H_3SC(O)N(CH_3)_2$ (22.9 mmol, 7.65 g) is slowly added to $LiAlH_4$ (109.4 mmol, 4.15 g) in diethyl ether (60 mL). The mixture is then refluxed for 12 h and left overnight at room temperature. The excess hydride is neutralized by dropwise addition of water, and the solution is then very slowly and with constant stirring poured into 1 L of acidified crushed ice. H_2SO_4 (2 mol/L) is added, and the resulting solid is filtered and recrystallized from hot methanol (3 g, 40% yield). ^1H NMR: δ 3.4 (1H, s, SH); 7.2−7.4 (13H, m, phenyl).

Diphenylmethylthiol was synthesized following the general Koenig et al. method:[27] Freshly distilled bromodiphenylmethane (27 mmol, 6.67 g) and thiourea (30 mmol, 2.3 g) are refluxed in 100 mL of ethanol under argon for 4 h; 30 mL of 2 M NaOH is then added, and the reflux is continued for an additional 2 h. After cooling, diluted HCl (37%) is added until pH 2. The thiol is extracted from the aqueous solution with dichloromethane. The organic phase is dried over $MgSO_4$, reduced to about 50 mL, and used as such (this thiol decomposes easily, and could not therefore be obtained in a pure state: the NMR shows residual peaks of ethanol, diethyl ether, and dichloromethane). ^1H NMR: δ 2.3 (1H, d, SH); 5.4 (1H, d, CH); 7.2−7.5 (10H, m, phenyl).

2,4,6-Triisopropylbenzylthiol was obtained by first preparing the 2,4,6-triisopropylbenzyl chloride,[28,29] which was then converted to the thiol by the Koenig et al. method.[27] 2,4,6-Triisopropylbenzene (73 mmol, 15 g) and chloromethyl methyl ether (181 mmol, 14.55 g) are dissolved in 50 mL of CS_2. The solution is then cooled to −5 °C, and $TiCl_4$ (33 mmol, 6.23 g) is slowly added. The mixture is left at room temperature for 4 h and then poured into 150 mL of ice−water. The organic phase is extracted with dichloromethane (4 × 50 mL) and dried over Na_2SO_4. Vacuum distillation (100 °C, 1 mmHg) produces 8.83 g of crystalline 2,4,6-triisopropylbenzyl chloride (48% yield). Mp: 32−34 °C. ^1H NMR: δ 1.24 (18H, m, CH_3); 2.86 (1H, spt, *p*-CH); 3.29 (2H, spt, *o*-CH); 4.73 (2H, s, CH_2Cl); 7.02 (2H, s, phenyl). Anal. Calcd for $C_{16}H_{25}Cl$: C, 76.01; H, 9.97. Found: C, 76.1; H, 10.5. 2,4,6-Triisopropylbenzyl chloride (29 mmol, 7.35 g) and thiourea (29 mmol, 2.2 g) are refluxed in ethanol/water (21 mL/3.5 mL) for 3 h. An aqueous solution of NaOH (57 mmol, 2.3 *g*, 3.8 mL) is then added, and the mixture is

(22) Lawson Daku, L. M. Etude de la protéine fer-soufre à haut potentiel de Chromatium vinosum et de composés modèles: structures électroniques dans les états d'oxidation $[4Fe\text{-}4S]^{2+}$ et $[4Fe\text{-}4S]^{3+}$ en relation avec les données d'aimantation et des mesures optiques à température variable. Thesis, Université Joseph Fourier, 1999.

(23) Antanaitis, B. C.; Moss, T. H. *Biochim. Biophys. Acta* **1975**, *405*, 262−279.

(24) Laskowski, E. J.; Frankel, R. B.; Gillum, W. O.; Papaefthymiou, G. C.; Renaud, J.; Ibers, J. A.; Holm, R. H. *J. Am. Chem. Soc.* **1978**, *100*, 5322−5337.

(25) Papaefthymiou, G. C.; Laskowski, E. J.; Frota-Pessôa,; Frankel, R. B.; Holm, R. H. *Inorg. Chem.* **1982**, *21*, 1725−1728.

(26) Bishop, P. T.; Dilworth, J. R.; Nicholson, T.; Zubieta, J. *J. Chem. Soc., Dalton Trans.* **1991**, 385−392.

(27) Koenig, N. H.; Sasin, G. S.; Swern, D. *Inorg. Chem.* **1958**, *23*, 1525−1530.

(28) Beets, M. G. J.; Meerburg, W.; Essen, H. V. *Recl. Trav. Chim. Pays-Bas* **1959**, *78*, 571.

(29) Tashiro, M.; Yamato, T.; Fukata, G. *J. Org. Chem.* **1978**, *43*, 1413−1420.

further refluxed under argon for 1.5 h. The solution is then cooled to 3 °C and acidified with concentrated HCl to pH 2. The white solid thus obtained is filtered off and rinsed with concentrated HCl and then water (200 mL). Drying overnight under vacuum provides 5.5 g of 2,4,6-triisopropylbenzylthiol (75% yield). Mp: 32−35 °C. ^{1}H NMR: δ 1.24 (18H, m, CH_3); 1.69 (1H, t, SH); 2.84 (1H, spt, *p*-CH3); 3.23 (2H, spt, *o*-CH); 3.81 (2H, d, CH_2SH); 6.99 (2H, s, phenyl). Anal. Calcd for $C_{16}H_{26}S$: C, 76.74; H, 10.46; S, 12.80. Found: C, 76.0; H, 10.2; S, 12.6.

2,4,6-Triphenylbenzylthiol was obtained by a four-step synthesis, which involved the successive preparation of the 2,4,6-triphenylbromobenzene,[30] the 2,4,6-triphenylbenzyl methyl ether, the 2,4,6-triphenylbenzyl chloride, and the 2,4,6-triphenylbenzylthiol.[27] Triphenylbenzene (108 mmol, 33.0 g) and bromine (12 mL) are dissolved in CS_2 (250 mL) and left to react for 12 h. Methanol (500 mL) is then added, and the mixture is left to stand for 2 days. 2,4,6-Triphenylbromobenzene is collected as a white precipitate and is recrystallized from hot ethanol. Mp: 129−131 °C. 2,4,6-Triphenylbromobenzene (34 mmol, 13 g) is dissolved in a mixture of diethyl ether/hexane (150 mL/30 mL). The solution is cooled with an ice-bath, and 17 mL of *n*-BuLi (2.5 mol/L in hexane) is slowly added over 40 min. At the end of the addition, the ice-bath is removed and the solution left to react for an additional 2 h. A solution of freshly distilled chloromethyl methyl ether (43 mmol, 3.4 mL) in 50 mL of diethyl ether is then added dropwise. The mixture is left to react overnight and is then treated with 25 mL of diluted HCl. The organic phase is collected, washed twice with water, and dried over $CaCl_2$. After evaporation of the solvent, the solid is recrystallized from hot hexane. 2,4,6-Triphenylbenzyl methyl ether (9.33 g) is collected (79% yield). Mp: 96−98 °C. ^{1}H NMR: δ 3.12 (3H, s, CH_3); 4.0 (2H, s, CH_2); 7.3−7.7 (17H, m, phenyl). Anal. Calcd for $C_{26}H_{22}O$: C, 89.11; H, 6.33. Found: C, 89.1; H, 6.4. 2,4,6-Triphenylbenzyl methyl ether (25 mmol, 8.73 g) is dissolved under argon in 44 mL of dichloromethane, and the solution is cooled to −80 °C. BCl_3 (25 mmol, 2 mL of a 1 mol/L solution in CH_2Cl_2) is then quickly added under argon, and the temperature of the mixture is left to reach room temperature overnight. After washing with 1% NaOH, then water, the organic phase is dried over $MgSO_4$. The solvent is evaporated, and the resulting solid is recrystallized from hot ethanol (6.5 *g*, 74% yield). Mp: 119 °C. ^{1}H NMR: δ 4.4 (2H, s, CH_2Cl); 7.3−7.7 (17H, m, phenyl). 2,4,6-Triphenylbenzyl chloride (126 mmol, 4.5 g) and thiourea (126 mmol, 0.96 g) are dissolved in 60 mL of ethanol and 2.5 mL of water and refluxed for 3 h. NaOH is then added and reflux is maintained for an additional 1.5 h. The reaction mixture is cooled to 5 °C with an ice-bath and acidified to pH 2 with concentrated HCl. The resulting white solid is filtered, rinsed with water, and dried under vacuum. Recrystallization from hot ethanol affords 3.41 g (76% yield) of pure 2,4,6-triphenylbenzylthiol. Mp: 120 °C. ^{1}H NMR: δ 1.5 (1H, t, SH); 3.63 (2H, d, CH_2); 7.3−7.6 (17H, m, phenyl). Anal. Calcd for $C_{25}H_{20}S$: C, 85.19; H, 5.72; S, 9.10. Found: C, 85.9; H, 5.9; S, 9.0.

2,4,6-Tri-*tert*-butylbenzylthiol was obtained by the same four-step synthesis as 2,4,6-triphenylbenzylthiolate, and involved the successive preparation of the 2,4,6-tri-*tert*-butylbenzenebromide,[31,32] the 2,4,6-tri-*tert*-butylbenzyl methyl ether,[32,33] the 2,4,6-tri-*tert*-butylbenzyl chloride,[33] and the 2,4,6-tri-*tert*-butylbenzylthiol.[27,30] Tri-*tert*-butylbenzene (previously dried under vacuum for 24 h) is dissolved in trimethyl phosphate (200 mmol, 50 g in 660 mL) at 90 °C. The temperature is then brought to 60−70 °C, and bromine (230 mmol, 11.8 mL) is added. The reaction mixture is kept in darkness at 65 °C for 30 h, then let back to room temperature, and 660 mL of ice-cold water is added. After extraction with hexane (5 × 100 mL), the organic phase is dried over $CaCl_2$ and the solvent removed. The final solid was recrystallized (at least 3 times) from hot ethanol (33 g, 50% yield). Mp: 173−175 °C. ^{1}H NMR: δ 1.29 (9H, s, p-*t*-Bu); 1.56 (18H, s, *o*-*t*-Bu); 7.39 (2H, s, phenyl). 2,4,6-Tri-*tert*-butylbenzenebromide (24.6 mmol, 8 g) is dissolved in diethyl ether (440 mL) under argon. The solution is cooled to 0 °C, and *n*-BuLi (30 mmol, 19.3 mL in hexane) is added dropwise over 30 min. After 2 h at room temperature, the solution is acidified with diluted HCl, and the organic phase is washed with water (3 times). It is then dried over $CaCl_2$ and stripped of the solvent. The raw product is recrystallized (at least twice) from hot ethanol (4.8 g, 70% yield). Mp: 85−87 °C. ^{1}H NMR: δ 1.27 (9H, s, *p*-*t*-Bu); 1.45 (18H, s, *o*-*t*-Bu); 3.32 (3H, s, OCH_3); 4.73 (2H, s, OCH_2); 7.39 (2H, s, phenyl). 2,4,6-Tri-*tert*-butylbenzyl methyl ether (13 mmol, 3.8 g) is dissolved in 20 mL of CH_2Cl_2 and cooled to −70 °C, and BCl_3 (13 mmol, 13 mL of a 1 mol/L solution in CH_2Cl_2) is added. After 30 min, the residual BCl_3 and the solvent are evaporated. The residue is dissolved in 50 mL of dry diethyl ether, and the solution is treated twice with 1% NaOH, then with water. The organic phase is dried over $MgSO_4$, and the solvent is removed. The final product is recrystallized from diethyl ether (3.4 g, 87% yield). Mp: 139−141 °C. ^{1}H NMR: δ 1.28 (9H, s, *p*-*t*-Bu); 1.52 (18H, s, *o*-*t*-Bu); 5.27 (2H, s, CH_2Cl); 7.39 (2H, s, phenyl). To 2,4,6-tri-*tert*-butylbenzyl chloride (6.45 mmol) is added a solution of thiourea (6.45 mmol, 0.49 g) in 20 mL of ethanol. The reaction mixture is left to reflux under argon for 3 h. NaOH (13 mmol, 0.8 mL of a 15 N solution) is added and the reflux continued for another 1.5 h. The mixture is then cooled to 3 °C, and H_2SO_4, 6 N, is added until pH 2. The resulting precipitate is filtered, rinsed with water, and dried under vacuum before recrystallization from hot ethanol (1 g, 55% yield). Mp: 106−109 °C. ^{1}H NMR: δ 1.30 (9H, s, *p*-*t*-Bu); 1.50 (*o*-*t*-Bu); 1.735 (1H, t, SH); 4.34 (2H, d, CH2); 7.33 (phenyl). Anal. Calcd for $C_{18}H_{30}S$: C, 78.08; H, 10.96; S, 10.96. Found: C, 78.6; H, 10.9; S, 10.0.

Complex Synthesis. The ligand-exchange method was used in all cases.[34] Compound **1** was prepared following a published procedure.[15] The general method for all the other compounds involves dissolving $(X)_2[Fe_4S_4(S\text{-}t\text{-}Bu)_4]$ (X = Et_4N and/or Ph_4P) in acetonitrile (1 g in 50 mL) and adding to it a solution of the desired ligand in dichloromethane (20 mL). After stirring overnight under a static vacuum, the solution is pumped to dryness. Unless otherwise stated, the black solid is briefly rinsed with toluene, then extensively rinsed with diethyl ether, and dried under vacuum. All clusters are soluble in most organic solvents, and therefore difficult to recrystallize.

Compound 2 is recrystallized from acetonitrile/ethanol. ^{1}H NMR: δ 1.25 (6H, s, NCH_2CH_3); 3.2 (4H, s, NCH_2); 6.3 (1H, *p*-H); 7.3 (6H, m, *o*′,*p*′-H); 7.8 (4H, m, *m*′-H); 8.3 (2H, *m*-H). Anal. Calcd for $C_{88}H_{92}N_2S_4Fe_4$: C, 63.76; H, 5.59; N, 1.69; S, 15.47. Found: C, 63.5; H, 5.7; N, 1.7; S, 15.4.

Compound 3 is recrystallized from acetonitrile/diethyl ether. ^{1}H NMR: δ 1.2 (6H, s, NCH_2CH_3); 3.12 (4H, s, NCH_2); 7.0−7.6 (10H,

(30) Kohler, E. P.; Blanchard, L. W. J. *J. Am. Chem. Soc.* **1935**, *57*, 367−370.
(31) Myhre, P. C.; Owen, G. S.; James, L. L. *J. Am. Chem. Soc.* **1968**, *90*, 2115−2123.
(32) Fraenkel, G.; Subramanian, S.; Chow, A. *J. Am. Chem. Soc.* **1995**, *117*, 6300−6307.
(33) Barclay, L. R. C.; Sonawane, H. R.; MacDonald, M. C. *Can. J. Chem.* **1972**, *50*, 281−290.
(34) Christou, G.; Garner, C. D. *J. Chem. Soc., Dalton Trans.* **1979**, 1093−1094.

m, phenyl); 11.3 (1H, s, CH). Anal. Calcd for $C_{68}H_{84}N_2S_4Fe_4$: C, 57.95; H, 6.01; N, 1.99; S, 18.20. Found: C, 57.5; H, 6.2; N, 19; S, 18.8.

Compounds 4 and 4′. Only **4** can be recrystallized from acetonitrile/diethyl ether. ^{1}H NMR of **4′**: δ 1.25 (6H, s, NCH_2-CH_3); 1.3 (6H, s, *p*-CH_3); 1.46 (12H, s, *o*-CH_3); 3.0 (1H, s, *p*-CH); 3.12 (4H, s, NCH_2); 3.8 (2H, s, *o*-CH); 7.2 (2H, s, phenyl); 14.4 (2H, s, CH_2). Anal. Calcd for **4**, $C_{112}H_{140}P_2S_4Fe_4$: C, 66.30; H, 6.96; S, 12.65; Fe, 11.01. Found: C, 66.4; H, 6.9; S, 12.7; Fe, 10.8.

Compounds 5 and 5′. Only **5′** can be recrystallized from acetonitrile/diethyl ether. ^{1}H NMR of **5′**: δ 1.25 (6H, s, NCH_2-CH_3); 3.2 (4H, s, NCH_2); 7.2−7.8 (17H, m, phenyl); 13.8 (2H, s, CH_2). Anal. Calcd for **5′**, $C_{116}H_{116}N_2S_4Fe_4$: C, 69.04; H, 5.79; N, 1.39; S, 12.71. Found: C, 69.1; H, 5.8; N, 1.4; S, 12.5.

Compound 6. ^{1}H NMR: δ 1.20 (6H, s, NCH_2CH_3); 1.33 (9H, s, *p*-*t*-Bu); 1.9 (18H, s, *o*-*t*-Bu); 2.90 (4H, s, NCH_2); 7.5 (2H, s, phenyl); 15.7 (2H, s, CH_2).

X-ray Structure Determination of 2. Dark brown single crystals were obtained by letting a concentrated solution of **2** in CH_3CN/CH_3OH stand for two weeks at room temperature. The compound crystallizes in the orthorombic space group *Pcca* with $a = 40.242(2)$ Å, $b = 19.422(1)$ Å, $c = 22.316(1)$ Å, $V = 17441(2)$ Å^3, $Z = 8$. Diffraction data were collected at $T = 193$ K on a three-circle diffractometer equipped with a Bruker SMART CCD area detector and graphite-monochromated Mo Kα radiation ($\lambda = 0.71073$ Å). The SMART and SAINT programs[35] were used for data collection and data processing. Absorption correction was performed using the SADABS software.[36] The SHELXTL 5.1 program[37] was used for structure solution and refinement. The cell parameters were obtained with intensities detected on three batches of 15 frames with a 300 s exposure time for each, and then refined using unique intensities with $I > 10\sigma(I)$ from all data. The data collection (crystal−detector distance: 6 cm, $1.46° \le \theta \le 23.27°$, 1323 frames (300 s exposure time) collected with 0.3° increments in ω for 3 settings of φ and θ; range of *hkl*: $-44 \le h \le +38$; $-20 \le k \le +21$; $-24 \le l \le +23$ (no detectable crystal decay after data collection)) gave 59849 intensities, of which 12442 were independent. The structure was solved by direct methods. All non-hydrogen atoms of the structure were found by difference Fourier syntheses and were refined anisotropically on F^2. Hydrogen atoms were treated as riding atoms. Final indices are $R = 0.0918$ and $R_w = 0.2457$ [$I > 2\sigma(I)$] with a residual electron density $\Delta\rho < 1.201$ e Å^{-3}. Only 1.5 NEt_4 entities could be identified, and residual peaks on the electron density map were tentatively interpreted as a water and methanol molecules with partial occupancies (disorder problems evidenced by the structure do not allow us to be confident regarding the assignment of these solvent molecules; this is especially true for the supposed water molecule since all manipulations were carried out under dry conditions). Further refinement of the structure requires the lowering of the symmetry from orthorhombic to triclinic. Such an additional work remains beyond the scope of the present studies, particularly since the structure of the $\mathbf{2}^{2-}$ anion is well resolved.

Electrochemical Experiments. Electrochemistry was performed with a Princeton Applied Research 273 potentiostat controlled by the Research Electrochemistry Software M270/250. Platinum working and counter electrodes were used. The reference Ag/AgI/I^- electrode was a silver wire immersed in a AgI-saturated CH_2Cl_2 solution containing the supporting electrolytes Bu_4NPF_6 (0.1 mol/L) and Bu_4NI (0.02 mol/L) and had a potential $E = -0.285$ mV vs SCE in CH_2Cl_2.

Magnetization Measurements. The reduced HiPIP of *C. vinosum* was purified and deuterated as previously described.[38] The deuteration of the protein sample allows elimination of the noise arising from the nuclear magnetization of the slowly relaxing water protons (nuclear spin $I = 1/2$) of water.[39] The magnetization data were collected on a 100 μL sample whose protein concentration was estimated, by optical measurements, to approximately 10 mmol/L in D_2O. Before measurements, the quartz sample holder was first left overnight in a 10% HF solution to eliminate potential ferromagnetic contaminants on its surface, then washed in distilled water, sonicated, and rinsed with distilled water. For the model compounds, samples of 13−43 mg were used: they were finely ground and put in sample holders made of highly pure aluminum plate. Magnetization data were collected on the protein sample by use of a SHE Corporation model 905 SQUID magnetometer, and on the model samples by use of a Quantum Design Magnetic Property Measurement System. Data were collected in the 4−300 K temperature range. The applied magnetic field strength took values greater than ($\ge$) 0.2 T in order to saturate potential ferromagnetic impurities and thus avoid the hysteresis they may contribute to at low field strengths.[39] The raw magnetization data were first corrected for the empty holder contribution recorded under the same conditions, and then from the diamagnetic and temperature independent paramagnetism contributions. The remaining paramagnetic contributions $M_{exp}(H, T) = \chi_{exp}(H, T) \times H$ were adjusted by minimization of the residual $\mathscr{R}$:

$$\mathscr{R}^2 = \frac{1}{N_{data} - N_{param}} \times \frac{\sum_i \sum_j [\chi_{th}(H_i, T_{ij}) - \chi_{exp}(H_i, T_{ij})]^2 \times {T_{ij}}^2}{\sum_i \sum_j [\chi_{th}(H_i, T_{ij})]^2 \times {T_{ij}}^2} \quad (1)$$

using the nearest-neighbor pivot method.[40] In eq 1, N_{data} and N_{param} correspond respectively to the number of experimental data and the number of parameters adjusted; their difference is the number of degrees of freedom available for a given fitting process. $\chi_{th}(H_i, T_{ij})$ represents the theoretical values of the susceptibility for an applied field strength H_i and a temperature T_{ij}. $\chi_{th}(H, T)$ reads

$$\chi_{th}(T, H) = n \times \chi_m(T) + n' \times \chi'_m(T) + TIC_H \quad (2)$$

The first term represents the contribution of n mol of a $[Fe_4S_4]^{2+}$ system whose molar paramagnetic susceptibility χ_m is given by eq 5. Impurities contribution is accounted for by the second term which represents, in the case of the reduced HiPIP, the signal arising from n' mol of a monomeric species of spin $1/2$, with a g factor equal to g_e and whose molar susceptibility χ'_m follows the Curie law. In the case of the model compounds, it corresponds to the contribution of n' mol of anisotropic high-spin ferric impurities whose anisotropy

(35) *SMART and SAINT Area-Detector Control and Integration Software*; Bruker Analytical X-Ray Instruments Inc.: Madison, WI, 1995.
(36) *SADABS, Bruker Area Detector Absorption Corrections Software*; Bruker Analytical X-Ray Systems: Wissembourg, France, 1998.
(37) Sheldrick, G. M. *SHELXTL-Plus*, version 5.1; Structure Determination Software Programs; Bruker Analytical X-ray Instruments Inc.: Madison, WI, 1998.
(38) Gaillard, J.; Albrand, J.-A.; Moulis, J.-M.; Wemmer, D. E. *Biochemistry* **1992**, *31*, 5632−5639.
(39) Day, R. P. *Methods Enzymol.* **1993**, *227*, 437−463.
(40) Serra, P.; Stanton, A. F.; Kais, S. *J. Chem. Phys.* **1997**, *106*, 7170−7177.

is accounted for by an axial zero field splitting parameter D.[41] Uncertainties on the diamagnetic and temperature independent paramagnetism corrections are also taken into account with the parameter TIC_H, a field dependent temperature independent correction.

Variable Temperature Optical Measurements. KBr pellets were used for the optical experiments. They were obtained by the intimate mixing of 200 mg of analytical grade KBr and the compounds in a quantity corresponding to a point of spatula. Absorption spectra were recorded on the pellet samples by use of a VARIAN CARY 2400 spectrometer for wavelengths ranging from 400 to 2600 nm and at nine different temperatures (10, 30, 60, 90, 130, 170, 210, 250, and 300 K). The sample temperature was controlled by helium gas flowing around the sample. The flow rate was adjusted with a Reciprotor pump. The rest of the cryogenic system consists of a circulating gas cryostat and an RGP 3000 temperature regulator, both made by the Société des Matériels Cryogéniques. The regulator was connected to a CLTS temperature sensor tied to a sample support tube designed by us. The pellets were put on a sample holder, also designed by us, which takes place on the sample support tube. Controls were carefully measured on KBR only disks that revealed disruptions at 490, 570, 640, 800, 1200, 1890, and 2190 nm, coming from the apparatus (Figure S1, Supporting Information).

Theoretical Considerations

$[Fe_4S_4]^{2+}$ systems are mixed-valence systems consisting formally of two ferrous and two ferric interacting monomeric fragments which are high-spin. Antiferromagnetic coupling results in a diamagnetic ground state which therefore cannot be characterized by electron resonance techniques. ^{57}Fe Mössbauer studies of the reduced HiPIP of *C. vinosum*[42] as well as of several biological and synthetic $[Fe_4S_4]^{2+}$ systems[4,43,44] show that the four iron sites can be divided into two totally delocalized mixed-valence pairs which are potentially equivalent. Within each pair, both sites are equivalent. The four iron sites may then be viewed as equivalent and as being of average $Fe^{2.5+}$ redox state. The observed equivalence of iron sites can be correlated with the crystallographic and resonance Raman (RR) data of the reduced HiPIP from *C. vinosum* and other biological or model $[Fe_4S_4]^{2+}$ systems which indicate that the $[Fe_4S_4]$ core presents a D_{2d} type distortion.[3,10,11,24,45−48] It was recently shown by Bominaar et al. that the interplay between exchange, double exchange, and vibronic coupling phenomena is responsible for the Jahn−Teller distortion of the $[Fe_4S_4]^{2+}$ core from T_d to D_{2d}; and that the diamagnetic D_{2d} ground state results from the antiferromagnetic coupling of mixed-valence pairs of maximum spin, the ferromagnetic coupling within the mixed-valence pairs being promoted by double exchange.[44]

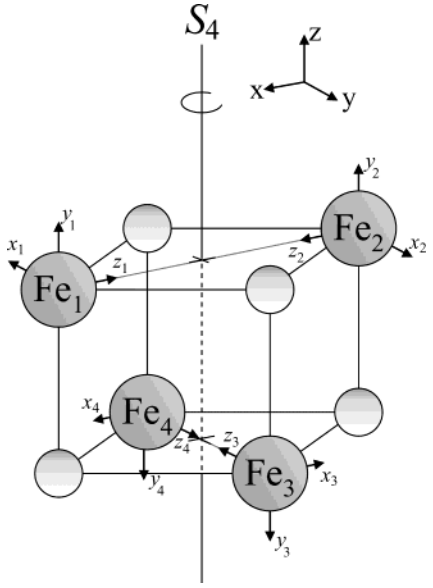

Figure 1. Schematic representation of the $[Fe_4S_4]$ core of $[Fe_4S_4]^{2+}$ systems assumed to be of ideal D_{2d} symmetry. The *x* and *y* directions correspond to the directions of direct Fe−Fe interactions within the Fe_1-Fe_2 and Fe_3-Fe_4 pairs, respectively.

Model for the Electronic Structure. For our studies, we make the assumption that the $[Fe_4S_4]^{2+}$ systems are of D_{2d} symmetry (Figure 1). The paramagnetic centers are modeled as two interacting equivalent mixed-valence pairs, Fe_1-Fe_2 and Fe_3-Fe_4. The interactions among the iron sites can then be parametrized with the following model Hamiltonian:

$$\mathscr{H} = \mathscr{H}_{xc} + \mathscr{H}_t \tag{3}$$

$$\mathscr{H}_{xc} = \sum_{[\kappa]} \mathscr{P}^{[\kappa]}[J(\sum_{i<j} \mathbf{S}_i^{[\kappa]}\cdot\mathbf{S}_j^{[\kappa]}) + \Delta J(\mathbf{S}_1^{[\kappa]}\cdot\mathbf{S}_2^{[\kappa]} + \mathbf{S}_3^{[\kappa]}\cdot\mathbf{S}_4^{[\kappa]})]\mathscr{P}^{[\kappa]}$$

$$\mathscr{H}_t = \beta\mathscr{P}_0 t_{12}\mathscr{P}_0 + \beta\mathscr{P}_0 t_{34}\mathscr{P}_0$$

$\mathscr{H}_{xc}$ refers to the isotropic exchange interactions within each of the four configurations [κ = *i*, *ii*, *iii*, *iv*] obtained by assigning each iron site a local Fe^{2+} or Fe^{3+} high-spin state ($S_i^{[\kappa]} = {}^5/_2, 2$).

[*i*]	[*ii*]	[*iii*]	[*iv*]
Fe_1^{2+}, Fe_2^{3+}	Fe_1^{3+}, Fe_2^{2+}	Fe_1^{2+}, Fe_2^{3+}	Fe_1^{3+}, Fe_2^{2+}
Fe_3^{2+}, Fe_4^{3+}	Fe_3^{2+}, Fe_4^{3+}	Fe_3^{3+}, Fe_4^{2+}	Fe_3^{3+}, Fe_4^{2+}

$\mathscr{P}^{[\kappa]}$ projects onto states originating from configuration [κ]. J is the interlayer coupling constant linking a site of one pair to a site of the other pair; the coupling constant within a pair is given by $J + \Delta J$. $\mathscr{H}_t$ is the double exchange interactions Hamiltonian, responsible for the electronic transfer inside each mixed-valence pair. β is the transfer integral. t_{ij} ($(i, j) \in \{(1, 2), (3, 4)\}$) operates within a mixed-valence pair, transferring the excess electron between sites Fe_i and Fe_j. Its action leads to the double occupation of either a magnetic orbital a_i centered on Fe_i or a magnetic orbital a_j centered on Fe_j, the magnetic orbitals a_i probably being mainly of d_{z^2} character[49,50] as this was shown by variable temperature MCD studies for valence-delocalized $[Fe_2S_2]^+$ clusters and $[Fe_2S_2]^+$ fragment containing systems.[51] $\mathscr{P}_0$ projects the electronic state resulting from an electronic transfer onto physical states respecting local Fe^{2+} or Fe^{3+} high-spin states.

An orthonormal basis of the electronic states space is the set of states $|S_{12}, S_{34}, S, M_S; [\kappa]\rangle$ arising from the configurations [κ] (κ =

(41) Contribution of high-spin ferric impurities ($S = {}^5/_2$) has been accounted for by the relation[54] $\chi'_m = (\chi_z + 2\chi_x)/3$, with $\chi_z = \mathscr{C} \times (1 + 9e^{-2\lambda} + 25e^{-6\lambda})/\mathscr{Z}$, $\chi_x = \mathscr{C} \times (9 + 8/\lambda - 11e^{-2\lambda}/2\lambda - 5e^{-6\lambda}/2\lambda)/\mathscr{Z}$, $\mathscr{C} = N_A g_e^2 \mu_B^2/(4k_B T)$, $\mathscr{Z} = 1 + e^{-2\lambda} + e^{-6\lambda}$, and $\lambda = D/k_B T$. D is the axial zero field splitting parameter.

(42) Middleton, P.; Dickson, D. P. E.; Johnson, C. E.; Rush, J. D. *Eur. J. Biochem.* **1980**, *104*, 289−296.
(43) Papaefthymiou, V.; Millar, M. M.; Münck, E. *Inorg. Chem.* **1986**, *25*, 3010−3014.
(44) Bominaar, E. L.; Hu, Z.; Münck, E.; Girerd, J.-J.; Borshch, S. A. *J. Am. Chem. Soc.* **1995**, *117*, 6976−6989.
(45) Carter, C. W., Jr.; Kraut, J.; Freer, S. T.; Alden, R. A. *J. Biol. Chem.* **1974**, *249*, 6339−6346.
(46) Berg, J. M.; Holm, R. H. In *Iron-Sulfur Proteins*; Spiro, T. G., Ed.; Wiley-Interscience: New York, 1982.
(47) Mascharak, P. K.; Hagen, K. S.; Spence, J. T.; Holm, R. H. *Inorg. Chim. Acta* **1983**, *80*, 157−170.
(48) Moulis, J.-M.; Meyer, J.; Lutz, M. *Biochemistry* **1984**, 6605−6613.

i, *ii*, *iii*, *iv*). S_{12} and S_{34} are the resulting spins of the mixed-valence pairs; they take values in $\{^1/_2, ^3/_2, ..., ^9/_2\}$. S and M_S refer respectively to the total electronic spin and its projection onto the *z*-axis (S takes values in {0, 1, ..., 9}). These states are eigenstates of $\mathscr{H}_{xc}$ associated with the eigenvalues:

$$E(S_{12}, S_{34}, S, M_S; [\kappa]) = \frac{J}{2}S(S+1) + \frac{\Delta J}{2}[S_{12}(S_{12}+1) + S_{34}(S_{34}+1)]$$

As the energies $E(S_{12}, S_{34}, S, M_S;[\kappa])$ depend only on the quantum numbers S, S_{12}, and S_{34}, we obtain that for fixed values of these numbers the $4(2S+1)$ states $|S_{12}, S_{34}, S, M_S; [\kappa]\rangle$ ($M_S = -S, ..., S$; $\kappa = i-iv$) are degenerate in the absence of the double exchange interactions. Diagonalization of $\mathscr{H}_t$ exploits the fact that it does not act upon the total electronic spin, thus coupling states with the same quantum numbers S and M_S, but also states with the same quantum numbers S_{12} and S_{34}: both numbers are good quantum numbers associated with the dimeric subunits Fe_1-Fe_2 and Fe_3-Fe_4. Consequently, given S_{12}, S_{34}, S, and M_S, $\mathscr{H}_t$ will only act within the subspace generated by the four states $|S_{12}, S_{34}, S, M_S; [\kappa]\rangle$ we note $|\kappa\rangle$ ($\kappa = i-iv$). Using the known results about the delocalization within an $Fe^{2+}-Fe^{3+}$ mixed-valence pair,[52,53] the matrix of $\mathscr{H}_t$ within this subspace reads

	$\|i\rangle$	$\|ii\rangle$	$\|iii\rangle$	$\|iv\rangle$
$\langle i\|$	0	$B(S_{12}+{}^1/_2)$	$B(S_{34}+{}^1/_2)$	0
$\langle ii\|$		0	0	$B(S_{34}+{}^1/_2)$
$\langle iii\|$			0	$B(S_{12}+{}^1/_2)$
$\langle iv\|$				0

with $B = -\beta/5$. Its diagonalization leads to the eigensystem of $\mathscr{H}_t$:

Eigenenergy:		Eigenstate:
$B[-(S_{12}+1/2)-(S_{34}+1/2)]$	$\Leftrightarrow$	$\underbrace{\frac{1}{2}[\|i\rangle - \|ii\rangle - \|iii\rangle + \|iv\rangle]}_{\|S_{12}, S_{34}, S, M_S; --\rangle}$
$B[(S_{12}+1/2)-(S_{34}+1/2)]$	$\Leftrightarrow$	$\underbrace{\frac{1}{2}[-\|i\rangle - \|ii\rangle + \|iii\rangle + \|iv\rangle]}_{\|S_{12}, S_{34}, S, M_S; +-\rangle}$
$B[-(S_{12}+1/2)+(S_{34}+1/2)]$	$\Leftrightarrow$	$\underbrace{\frac{1}{2}[-\|i\rangle + \|ii\rangle - \|iii\rangle + \|iv\rangle]}_{\|S_{12}, S_{34}, S, M_S; -+\rangle}$
$B[(S_{12}+1/2)+B_{34}(S_{34}+1/2)]$	$\Leftrightarrow$	$\underbrace{\frac{1}{2}[\|i\rangle + \|ii\rangle + \|iii\rangle + \|iv\rangle]}_{\|S_{12}, S_{34}, S, M_S; ++\rangle}$

Finally, we obtain that the stationary states of $[Fe_4S_4]^{2+}$ systems are states $|S_{12}, S_{34}, S, M_S; \epsilon_{12}\epsilon_{34}\rangle$ ($\epsilon_{ij} = \pm$) associated with the energies:

$$E(S_{12}, S_{34}, S; \epsilon_{12}\epsilon_{34}) = \frac{J}{2}S(S+1) + \frac{\Delta J}{2}[S_{12}(S_{12}+1) + S_{34}(S_{34}+1)] + B[\epsilon_{12}(S_{12}+{}^1/_2) + \epsilon_{34}(S_{34}+{}^1/_2)] \quad (4)$$

Magnetic Susceptibility. The molar susceptibility of powder and frozen solution samples of the coupled $[Fe_4S_4]^{2+}$ systems reads[54]

$$\chi_m(T) = \frac{N_A g_e^2 \mu_B^2}{3k_B T} \times \frac{\sum_{\mathscr{E}(S_{12}, S_{34}, S; \epsilon_{12}\epsilon_{34})} S(S+1)(2S+1)\exp(-E(S_{12}, S_{34}, S; \epsilon_{12}\epsilon_{34})/k_B T)}{\sum_{\mathscr{E}(S_{12}, S_{34}, S; \epsilon_{12}\epsilon_{34})} (2S+1)\exp(-E(S_{12}, S_{34}, S; \epsilon_{12}\epsilon_{34})/k_B T)} \quad (5)$$

where the system g factor is taken equal to the free electron one, g_e. N_A is the Avogadro number, k_B is the Boltzmann constant, and μ_B is the Bohr magneton. The summations take place over all 440 subspaces $\mathscr{E}(S_{12}, S_{34}, S; \epsilon_{12}\epsilon_{34})$. The adjustment of the magnetization data using eq 5 allows probing of the electronic structure of $[Fe_4S_4]^{2+}$ systems within the exchange and double exchange theoretical framework.

Optical Properties. The electronic delocalization phenomenon within the mixed-valence pairs should give rise to spin and electric dipole-allowed one-electron transitions between a state $|S_{12}, S_{34}, S, M_S; \epsilon_{12}\epsilon_{34}\rangle$ and states $|S_{12}, S_{34}, S, M_S; -\epsilon_{12}\epsilon_{34}\rangle$, $|S_{12}, S_{34}, S, M_S; \epsilon_{12}-\epsilon_{34}\rangle$, at energies

$$E_{opt} = 2|B|(S_{ij}+{}^1/_2) = \frac{2}{5}|\beta|(S_{ij}+{}^1/_2), \quad (i,j) \in \{(1,2),(3,4)\} \quad (6)$$

for fixed values of S_{12}, S_{34}, S, M_S, ϵ_{12}, and ϵ_{34}. Such transitions are predicted to be polarized along the *x* and *y* directions which are the directions of iron−iron interactions within the Fe_1-Fe_2 and Fe_3-Fe_4 mixed-valence pairs, respectively (Figure 1). From a molecular orbital viewpoint, they correspond to one-electron transitions between bonding ($\sigma_{ij}(+)$) and antibonding ($\sigma_{ij}(-)$) orbitals centered on the mixed-valence pairs, and which results from the σ overlap of the magnetic orbitals a_i and a_j ($\sigma_{ij}(\pm) \propto [a_i \pm a_j]$).

Results

Magnetization Studies of the Reduced HiPIP from *Chromatium vinosum*. In order to extract the weak paramagnetic contribution from the bulk diamagnetic signal, we adopted the approach developed by Day and co-workers,[39,55] and we used a sample of approximately 10 mM (optical measurements) protein concentration, which led to the high-quality data shown in Figure 2. Data are displayed in Figure 2 as isofield curves corresponding to the product of the sample susceptibility χ_{sam} by temperature, plotted against temperature. Superposition of the three isofield curves guarantees that the sample magnetization response is linear in field for the strengths of field used. The shape of the curves confirms the well-known antiferromagnetic behavior of this system: the $\chi_{sam}T$ product is constant and nearly null below 70 K. This indicates a singlet electronic ground state and the exclusive population of singlet state(s). The increase observed above 70 K corresponds to the progressive popula-

(49) Gamelin, D. R.; Bominaar, E. L.; Kirk, M. L.; Wieghardt, K.; Solomon, E. I. *J. Am. Chem. Soc.* **1996**, *118*, 8085−8097.
(50) Gamelin, D. R.; Bominaar, E. L.; Mathonière, C.; Kirk, M. L.; Wieghardt, K.; Girerd, J.-J.; Solomon, E. I. *Inorg. Chem.* **1996**, *35*, 4323−4335.
(51) Johnson, M. K.; Duin, E. C.; Crouse, B. R.; Golinelli, M.-P.; Meyer, J. In *Spectroscopic Methods in Bioinorganic Chemistry*; Solomon, E. I., Hodgson, K. O., Eds.; American Chemical Society: Washington, DC, 1998; Vol. 692.
(52) Papaefthymiou, V.; Girerd, J.-J.; Moura, I.; Münck, E. *J. Am. Chem. Soc.* **1987**, *109*, 4703−4710.
(53) Blondin, G.; Girerd, J.-J. *Chem. Rev.* **1990**, *90*, 1359−1376.
(54) Kahn, O. *Molecular Magnetism;* VCH: New York, 1993.
(55) Day, E. P.; Kent, T. A.; Lindhal, P. A.; Münck, E.; Orme-Johnson, W. H.; Roder, H.; Roy, A. *Biophys. J.* **1987**, *52*, 837−853.

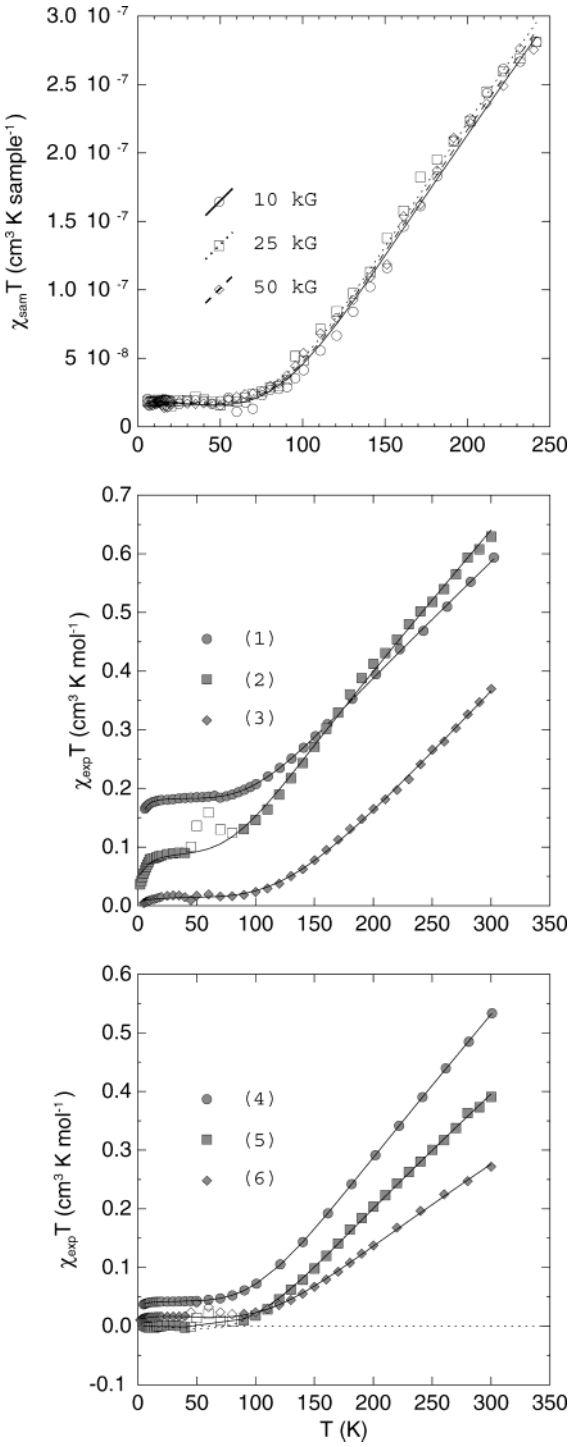

Figure 2. (top) Product of the sample susceptibility of reduced HiPIP from *C. vinosum* by temperature plotted against temperature: experimental isofield curves correspond to 1 *T* (circles), 2.5 *T* (squares), and 5 *T* (triangles); the lines correspond to the theoretical curves generated by the best fit parameters given in Table 1A (solid, 1 *T*; dotted, 2.5 *T*; dashed, 5 *T*). (middle and bottom) Product of the molar susceptibility by temperature plotted against temperature for compounds **1**−**6**: the lines correspond to the theoretical curves generated by the best fit parameters (see Table 1A).

tion of excited state(s) of higher spin multiplicity. The almost zero value of $\chi_{sam}T$ below 70 K reveals the presence of paramagnetic impurities in weak concentration. This value ($\sim 1.9 \times 10^{-8}$ cm^3 K sample^{-1}) corresponds approximately to $n' \sim 50$ nmol ($\sim$0.5 mM) of monomeric species of spin $^1/_2$ obeying the Curie law.[56] This residual paramagnetic signal may arise from eventual ferric impurities (not detected by the EPR control of the sample), but certainly contains background signals (e.g., the nuclear paramagnetism of deuterons and protons not exchanged).[55]

At first the data have been fitted by letting float all parameters as follows: $n \in [0.6, 1.4]$ μmol, $J \in [-600, 600]$ cm^{-1}, $\Delta J \in [-600, 600]$ cm^{-1}, $B \in [0, 2000]$ cm^{-1}, $n' \in [0.02, 0.08]$ μmol, and $TIC_H \in [-10^{-10}, 10^{-10}]$ cm^3 sample^{-1}. Minimization calculations always led to $n' \approx 50$ nmol as expected, and also to $|TIC_H| \approx 2-8 \times 10^{-11}$ cm^3 sample^{-1}. Such small TIC values indicate that corrections were correctly performed on the raw magnetization data. The precise determination of these parameters comes from the fact that they are mainly fixed by the low-temperature data given that eq 2 reduces to $\chi_{th}(T, H) \approx n'\chi_m'(T) + TIC_H$ for such temperatures. The *J* values were still positive, confirming the antiferromagnetic behavior of the reduced HiPIP. Furthermore, they all were of the order of 300 cm^{-1}, showing that the *J* parameter proves to be primarily fixed by the temperature above which one experimentally observes the significant population of the first excited paramagnetic state, actually a triplet located at *J* above the diamagnetic ground state. Possible best values of *J* and of the parameters *n*, ΔJ, and *B* are then simultaneously determined by the behavior of the $\chi_{sam}T$ curves above this temperature threshold of 70 K. The best parameter set which has been obtained corresponds to a residual of $\mathcal{R} = 3.19 \times 10^{-3}$ and to parameter values of $n = 0.80$ μmol, $J = 303$ cm^{-1}, $\Delta J = 527$ cm^{-1}, $B = 94$ cm^{-1}, $n' = 48$ nmol, and $10^{11} \times TIC_H = -3.3, +0.9, -1.6$ cm^3 sample^{-1} for $H = 10, 25, 50$ kG, respectively. However, this solution clearly is unphysical as it neglects the double exchange phenomenon, and leads to ground and lowest lying excited states[57] characterized by antiferromagnetically coupled mixed-valence pairs because of the high ΔJ value. We therefore dismiss such a result.

Subsequent minimization calculations have been performed with *B* constrained to values greater than 400 cm^{-1} to avoid the attractive basin associated with the rejected solution and also avoid similar unphysical solutions characterized by vanishing *B* and high ΔJ values (see FigureS2, Supporting Information). Very satisfactory results have been obtained. They correspond to residuals $\mathcal{R}$ of $\sim 3.5 \times 10^{-3}$ and well-determined values of parameters $n \approx 0.7$ μmol and $J \approx 280$ cm^{-1}. However, we noted during these calculations that, while the double exchange parameter *B* tends to take

(56) For a monomeric species of spin *S* whose paramagnetic behavior obeys the Curie law, the product of its molar susceptibility by temperature reads $\chi T(g_e^2/g^2) = S(S+1)/2$, where g_e and *g* are the Landé factor for the free electron and the species, respectively. Assuming $g = g_e$, we have $\chi T = 0.375$ when $S = {}^1/_2$ and $\chi T = 4.375$ when $S = {}^5/_2$.

(57) For $J = 303$ cm^{-1}, $\Delta J = 527$ cm^{-1}, and $B = 94$ cm^{-1}, the ground level of the reduced HiPIP from *C. vinosum* is the diamagnetic $\mathcal{E}(S_{12} = {}^1/_2, S_{34} = {}^1/_2, S = 0; --)$ level. The lowest lying excited energy levels are (given with their energies relative to the ground level) $\mathcal{E}(S_{12} = {}^1/_2, S_{34} = {}^1/_2, S = 0; \pm\mp)$ at $2B$ (188 cm^{-1}); $\mathcal{E}(S_{12} = {}^1/_2, S_{34} = {}^1/_2, S = 1; --)$ at J (303 cm^{-1}); $\mathcal{E}(S_{12} = {}^1/_2, S_{34} = {}^1/_2, S = 0; ++)$ at $4B$ (376 cm^{-1}); $\mathcal{E}(S_{12} = {}^1/_2, S_{34} = {}^1/_2, S = 1; \pm\mp)$ at $J + 2B$ (491 cm^{-1}); $\mathcal{E}(S_{12} = {}^1/_2, S_{34} = {}^1/_2, S = 1; ++)$ at $J + 4B$ (679 cm^{-1}); $\mathcal{E}(S_{12} = {}^3/_2, S_{34} = {}^1/_2, S = 1; --)$; and $\mathcal{E}(S_{12} = {}^1/_2, S_{34} = {}^3/_2, S = 1; --)$ at $J - B + 3\Delta J/2$ (999.5 cm^{-1}).

any value in [400, 2000] cm^{-1}, it remains strongly correlated with ΔJ, ΔJ taking negative values and therefore favoring, as B does, ferromagnetic coupling within the mixed-valence pairs. Inspection of the resulting energy ladders revealed a same description of the electronic structure of the reduced HiPIP, namely, the three levels $\mathcal{E}(S_{12} = {}^9/_2, S_{34} = {}^9/_2, S; --)$, $S \in \{0, 1, 2\}$, as the lowest lying and mainly populated levels. The fact that these levels, with mixed-valence pairs of maximum spin, constitute the mainly populated ones within the available temperature range explains why it turns out to be impossible to obtain the respective values of parameters B and ΔJ. We have therefore adopted a simpler approach which consists of setting ΔJ to zero.[58,59] In this case, the value obtained for J corresponds to the average value $J_{av} = (4J + 2(J + \Delta J))/6 = J$ while double exchange becomes actually accounted for by the effective double exchange parameter $B_{\Delta J=0}$ (for convenience we shall drop the "$\Delta J = 0$" subscript and use it when one needs to distinguish between the effective and the very double exchange parameter). The residual $\mathcal{R}$ has been minimized repeatedly by fitting the susceptibility data with fixed values of n and B which have been varied by increments of 0.01 μmol and 100 cm^{-1}, and with the other parameters left free. Figure 3 shows the $\mathcal{R} = \mathcal{R}(n, B)$ and $J = J(n, B)$ surfaces for $n \in [0.6, 0.8]$ μmol and $B \in [500, 1900]$ cm^{-1}. The error map does not present a pronounced minimum but rather exhibits a valley that is narrow along the n direction and flat along B. In fact, each $\mathcal{R}(n, B)$ curve associated with a given B value displays a minimum and the trajectory of this minimum merges (within the accuracy limits provided by the numerical grid used) with the $\mathcal{R}(n = 0.68\ \mu\text{mol}, B)$ curve for $B \geq 1100$ cm^{-1}. This can be seen from Figure 4, which gives the plots of the best values obtained for the residual and the n and J parameters at fixed B values (plots against B of the best n' and TIC_H values are also given, Figure S3, Supporting Information). The amount of $[Fe_4S_4]^{2+}$ molecules thus determined, $n = 0.68(1)$ μmol, compares relatively well with the one estimated by optical measurements ($\sim$1 μmol).[60] Because of the lack of a well-defined minimum along the B, it turns out to be impossible to deduce a definitive B value from the fitting of the susceptibility data. Optimal B values however correspond to values greater than 1400 cm^{-1} since the $\mathcal{R}(n = 0.68\ \mu\text{mol}, B)$ curve, that proves to be a decreasing function of B, hardly differs from the value of 3.50×10^{-3} for $B \geq 1400$ cm^{-1} (Figure 4). The domain defined by $n = 0.68(1)$ μmol and $B \geq 1400$ cm^{-1} leads to an optimal J value of $J = 282(2)$ from the reading of the $J(n, B)$ data. The J surface (Figure 3) reveals that n and J are positively correlated and also that, for fixed n, the J value becomes almost independent of B for a sufficiently high value of this parameter. This latter fact is a consequence of the nature of the thermally accessible levels which no more

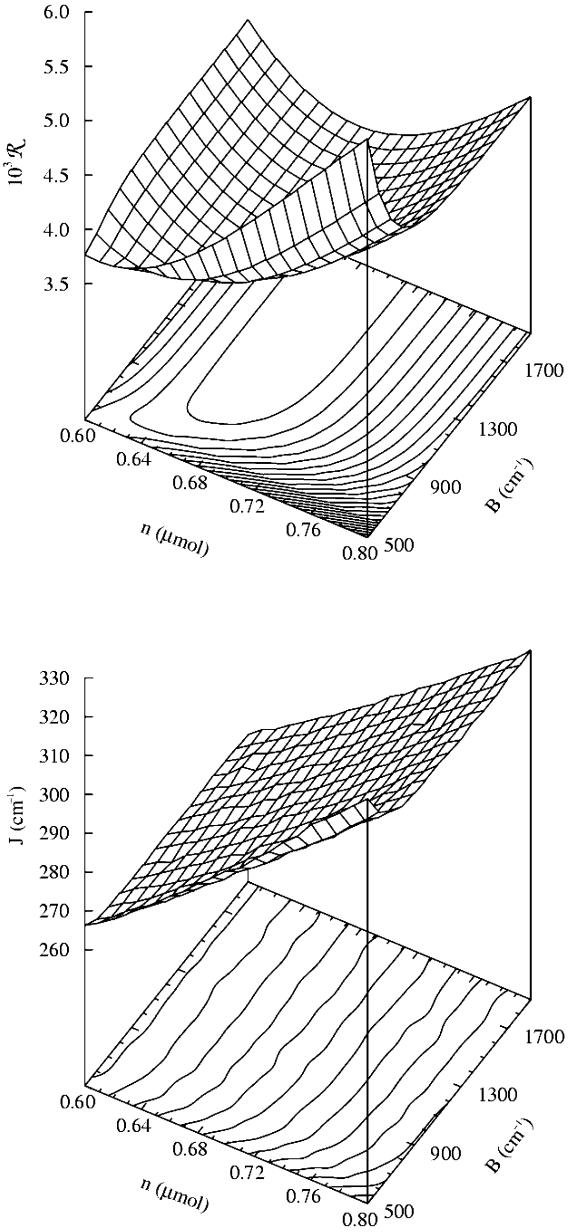

Figure 3. Error map (top) and $J = J(n, B)$ surface (bottom) constructed by fitting the susceptibility data of the reduced HiPIP of *C. vinosum* for fixed values of n and B (with ΔJ kept fixed to zero).

(58) Noodleman, L. *Inorg. Chem.* **1988**, *27*, 3677−3679.
(59) Jordanov, J.; Roth, E. K. H.; Fries, P. H.; Noodleman, L. *Inorg. Chem.* **1990**, *29*, 4288−4292.
(60) Due to the high sensitivity of SQUID magnetometers, the determination of the quantity n of $[Fe_4S_4]^{2+}$ proteins from magnetization data is a robust approach, far more reliable than a determination based on electronic absorption data. One must, however, note in the case of the $[Fe_4S_4]^{2+}$ systems that the determination of n from the fit of the susceptibility curves relies on the population of excited paramagnetic states (see eq 5). Hence the value of n is likely to be affected by the nature of the model used to describe the electronic structure. One factor that may influence n is the (reasonable) assumption that the system g factor is independent of the nature of the paramagnetic states and equal to g_e. Another source of influence that is not accounted for is the presence of vibrational levels on the energy ladder. The contribution of the κth electronic state $\mathcal{E}(S_{12}, S_{34}, S; \epsilon_{12}\epsilon_{34})$ to the numerator and denominator of eq 5 should indeed be multiplied by $Z_{vib,\kappa}(T)$, its associated vibrational partition function. The equality of the $Z_{vib,\kappa}$ functions implied by eq 5 is equivalent to neglecting the geometry changes in the electronic states. Whereas such an assumption seems reasonable for electronic states which only differ on the total electronic spin S and probably also on the spin quantum numbers S_{12} and S_{34}, it surely breaks down for states with different quantum numbers ϵ_{12} and ϵ_{34} as these numbers reflect the bonding or antibonding character of the orbitals occupied by the excess electrons. Results, however, show that all populated states are characterized by $\epsilon_{12} = \epsilon_{34} = -1$, so that the use of eq 5 remains justified. Finally, keeping in mind the limitations due to the sensible assumptions made about the isotropic g factor and the molecular geometry, one can be quite confident about the n value deduced from the magnetization data.

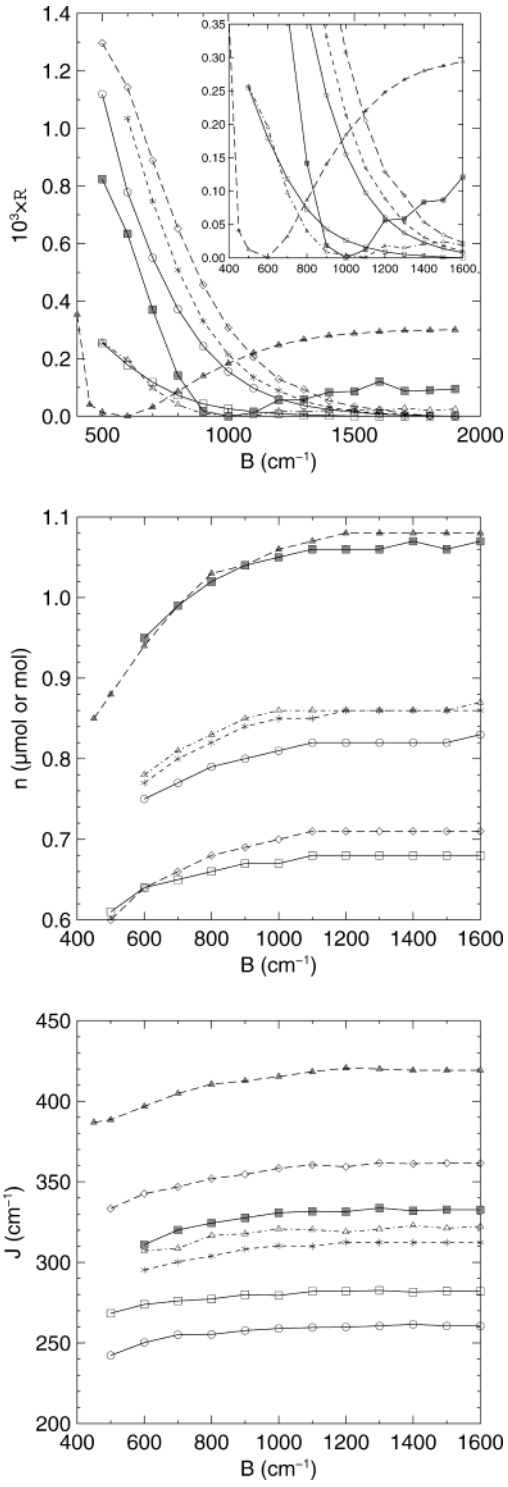

Figure 4. Best values of the residual $\mathscr{R}$ and of the *n* and *J* parameters obtained for fixed *B* values (with ΔJ kept fixed to zero). The curves are plotted for the reduced HiPIP from *C. vinosum* (squares) and the model compounds **1** (triangles), **2** (circles), **3** (filled triangles), **4** (filled squares), **5** (asterisks), and **6** (diamonds) ($\mathscr{R}$ curves have been shifted in order to set their minima to zero; true minimum values are given in Table 1A).

evolves with increasing *B* values. The positive correlation simply indicates that a too low (respectively too high) value of *n* must be compensated by a decrease (respectively increase) of *J* so as to put paramagnetic excited states lower (respectively higher) in energy and thus keep the theoretical χT curves as close as possible to the experimental ones, especially for the elevated temperatures. It is also observed in Figure 4 wherein the *n* and *J* curves show the same behavior. Table 1A summarizes the optimum values obtained for the residual and for the *n*, *J*, and *B* parameters. The fit corresponding to these optimal parameter values is shown in Figure 2 and, as expected from the low residual ($\mathscr{R} = 3.50 \times 10^{-3}$)[61] of Table 1A, one observes a very good agreement between the experimental and theoretical data. In Figure 5, the lowest lying energy levels of the reduced HiPIP from *C. vinosum* are given as deduced from the valuesof parameters *J* and *B* in Table 1A (Figure 5A), as well as the temperature dependence of their thermal populations $p\{(S_{12}, S_{34}, S; \epsilon_{12}\epsilon_{34}), T\}$ (Figure 5B).

Table 1. Parameter Values Obtained by Fitting the Magnetization Data of the Reduced *C. vinosum* HiPIP and of the Model Compounds[a]

(A) Optimal Values Deduced from the Error Maps' Regions of Smallest *R* Values

	n (mol)	*J* (cm^{-1})	*B*[b] (cm^{-1})	ΔJ (cm^{-1})	10^3R
reduced HiPIP	$0.68(1) \times 10^{-6}$	282(2)	≥1400	0[c]	3.50
1	0.86(1)	320(3)	1100(100)	0[c]	1.00
2	0.83(1)	261(2)	≥1500	0[c]	3.91
3	0.94(1)	397(8)	600(100)	0[c]	3.38
4	1.05(1)	331(2)	1000(100)	0[c]	0.44
5	0.86(1)	312(2)	≥1500	0[c]	2.33
6	0.72(1)	362(2)	≥1600	0[c]	2.90
reduced HiPIP	$0.68(1) \times 10^{-6}$	282(2)	0[c]	≤−350	3.50

(B) Values Deduced from Fit Results[d]

	n (mol)	*J* (cm^{-1})	*B*[b] (cm^{-1})	ΔJ (cm^{-1})	10^3R
reduced HiPIP	$0.66-0.68 \times 10^{-6}$	277−282	≥800	0[c]	3.50−3.57
1	0.84−0.88	317−324	≥800	0[c]	1.00−1.04
2	0.81−0.83	259−261	≥1000	0[c]	3.91−4.06
3	0.92−0.96	393−401	500−700	0[c]	3.38−3.41
4	1.03−1.07	324−334	≥800	0[c]	0.44−0.58
5	0.84−0.86	308−312	≥900	0[c]	2.33−2.66
6	0.70−0.72	358−362	≥1000	0[c]	2.90−3.21

[a] See also text. [b] *B* kept positive. [c] Kept fixed. [d] Fit results have been obtained for *B* values other than the optimal ones. The *n* values for the fit results differ from the optimal *n*'s by at most ±0.02 μmol for the reduced HiPIP and ±0.02 mmol for the model compounds.

$$p\{(S_{12}, S_{34}, S; \epsilon_{12}\epsilon_{34}), T\} = \frac{(2S+1)\exp[-E(S_{12}, S_{34}, S; \epsilon_{12}\epsilon_{34})/k_BT]}{\sum_{\mathscr{E}(S'_{12},S'_{34},S'>;\epsilon'_{12}\epsilon'_{34})} (2S'+1)\exp[-E(S'_{12}, S'_{34}, S'; \epsilon'_{12}\epsilon'_{34})/k_BT]} \quad (7)$$

Since double exchange promotes ferromagnetic coupling within mixed-valence pairs, it appears that the concomitant

(61) A better agreement was actually observed when ΔJ has been allowed to float: $\mathscr{R} = 3.40 \times 10^{-3}$, $(J, \Delta J, B) = (303, 527, 94)$ cm^{-1}. This slightly better quality of the fit can be understood by noting that the associated energy ladder[57] displays, in addition to a singlet ground level, low-lying excited singlet and triplet levels whose thermal population evolution in fact may help reproduce the competitive population of vibrational levels of ground and excited electronic states. This is a phenomenon which contributes to the slightly sigmoidal curvature observed for the $\chi_{sam}T$ curves at high temperatures but which is not accounted for by the theoretical model used.

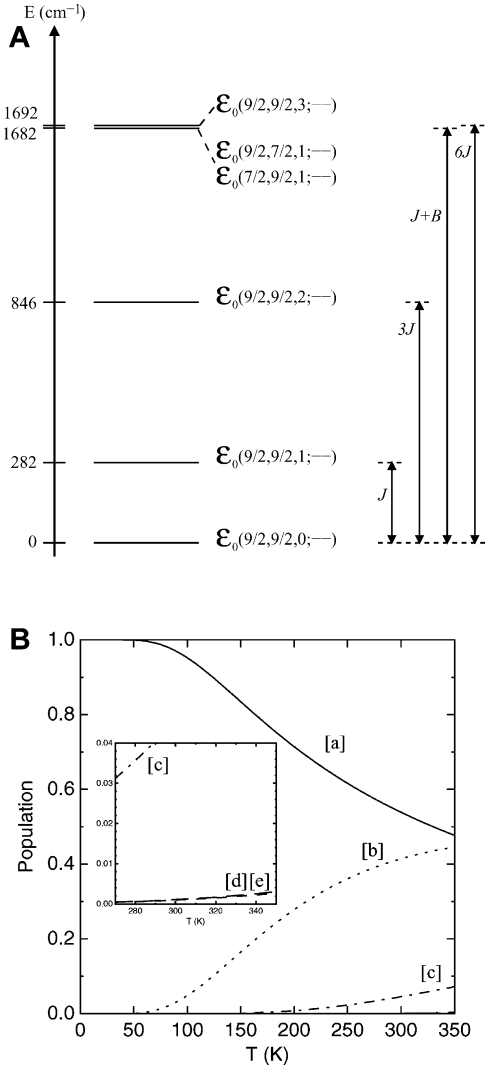

Figure 5. (A) The five lowest lying energy levels of the reduced HiPIP from *C. vinosum* (after the optimal *J* and *B* values of Table 1A). (B) Temperature dependence of their thermal population: (a) $\mathcal{S}(S_{12} = {}^9/_2, S_{34} = {}^9/_2, 0; --)$; (b) $\mathcal{S}(S_{12} = {}^9/_2, S_{34} = {}^9/_2, 1; --)$; (c) $\mathcal{S}(S_{12} = {}^9/_2, S_{34} = {}^9/_2, 2; --)$; (d) $\mathcal{S}(S_{12} = {}^9/_2, S_{34} = {}^7/_2, 1; --)$ and $\mathcal{S}(S_{12} = {}^7/_2, S_{34} = {}^9/_2, 1; --)$; (e) $\mathcal{S}(S_{12} = {}^9/_2, S_{34} = {}^9/_2, 3; --)$.

gain of delocalization energy is responsible for the stabilization of the three levels $\mathcal{S}(S_{12} = {}^9/_2, S_{34} = {}^9/_2, S; --)$, $S \in \{0, 1, 2\}$. The diamagnetic level $\mathcal{S}(S_{12} = {}^9/_2, S_{34} = {}^9/_2, S = 0; --)$ is the ground level. It is the only populated level below 70 K, in agreement with experimental observations. The paramagnetic properties of the reduced HiPIP from *C. vinosum* appearing above 70 K are due to the population of the triplet level $\mathcal{S}(S_{12} = {}^9/_2, S_{34} = {}^9/_2, S = 1; --)$. The quintet level $\mathcal{S}(S_{12} = {}^9/_2, S_{34} = {}^9/_2, S = 2; --)$ becomes populated above 200 K and then also contributes to the system's paramagnetic properties. Population of this level remains weak in comparison with those of the two levels lying below; however, its contribution to the paramagnetic properties cannot be neglected, especially at 300 K, since the contribution of a level of spin *S* to the susceptibility is proportional to $S(S + 1)(2S + 1)$ (see eq 5). Finally, one can infer from the optimum *J* and *B* values of Table 1A that the three electronic levels $\mathcal{S}(S_{12} = {}^9/_2, S_{34} = {}^9/_2, S; --)$, $S \in \{0, 1, 2\}$, are the only ones populated over the 0−300 K temperature range which is commonly used to study the reduced HiPIP from *C. vinosum*. They are therefore the onlyones responsible for the observed physicochemical properties of the reduced HiPIP over this temperature range. It is also interesting to note that the gaps between the three energy levels simply obey the Landé rule.

An alternative Heisenberg only approach has also been used for the data analysis. To proceed, an error map has been constructed over the $\{n, \Delta J\}$ parameter subset by varying *n* and ΔJ with increments of 0.01 μmol and 25 cm^{-1}, respectively. The surface displays two valleys (one for the positive ΔJ values and the other for the negative ones) that both are narrow along the *n* direction and large along ΔJ (Figure S2). The valley in the direction of the positive ΔJ values leads to solutions which are unphysical as they correspond to too high values of the coupling constant within the mixed-valence pairs, the pairs being also antiferromagnetically coupled in the ground and lowest lying excited states. Interestingly, negative ΔJ values promote the ferromagnetic coupling within the mixed-valence pairs like the double exchange phenomenon does. The optimal solutions associated with the negative ΔJ values are presented in the second part of Table 1A. The residual $\mathcal{R}$ value shows that the quality of the fit is identical to the one obtained with the exchange and double exchange approach. Moreover, the values of *n* and *J* obtained within both theoretical frameworks are identical and, given the optimum ΔJ values, the lowest lying and only populated levels deduced from the pure exchange approach are identical to the ones given in Figure 5.[62] There is, however, a significant physical difference between both energy ladders: the degeneracy of each energy level gets multiplied by 4 in the pure Heisenberg case because this approach does not account for the electronic delocalization. Therefore, it is important to keep in mind that a comparison between exchange parameters originating from both approaches is meaningless.[59] The similarities between the results obtained with both theoretical frameworks are related to the covariance between *B* and ΔJ which reads as follows:[63] for the set of subspaces to which the lowest lying levels belong, characterized by $S_{ij} \in \{{}^9/_2, {}^7/_2\}$ with $(i, j) \in \{(1, 2), (3, 4)\}$ (see Figure 5), similar energy ladders are obtained within this set with both approaches, provided that $|B_{\Delta J=0}| = {}^9/_2 \times |\Delta J_{B=0}|$ is verified. This actually corresponds to our situation as, for instance, we have for the minimum values reported in Table 1A for $|B_{\Delta J=0}|$ and $|\Delta J_{B=0}|$, $|B_{\Delta J=0}|_{\min} = 4.0(4) \times |\Delta J_{B=0}|_{\min}$ (the equality does not strictly match the covariance relation because $|B_{\Delta J=0}|_{\min}$ and $|\Delta J_{B=0}|_{\min}$ are determined with uncertainties that correspond to the grid sizes, 100 and 25 cm^{-1} respectively). In order to break the covariance relation, a state such as $S_{ij} = {}^5/_2$ ($(i, j) \in \{(1, 2), (3, 4)\}$) should be thermally accessible. This is not our case since, within the exchange and double exchange framework, we obtain that the first states verifying $S_{ij} = {}^5/_2$ belong to

(62) The three lowest energy levels correspond to the subspaces given by the direct sums: $\oplus\oplus\, \mathcal{S}(S_{12} = {}^9/_2, S_{34} = {}^9/_2, S; \epsilon_{12}\epsilon_{34})$, with $S = 0$, 1, 2.

(63) Crozet, M.; Chaussade, M.; Bardet, M.; Emsley, L.; Lamotte, B.; Mouesca, J.-M. *J. Phys. Chem. A* **2000**, *104*, 9990−10000.

the degenerated subspaces $\mathcal{S}(S_{12} = {}^9/_2, S_{34} = {}^5/_2, S = 2; --)$ and $\mathcal{S}(S_{12} = {}^5/_2, S_{34} = {}^9/_2, S = 2; --)$, and that they are located high in energy: at $2B + 3J$ above the ground level and at $2B$ above the first populated quintet subspace. Thus, even though a pure Heisenberg approach (with $\Delta J < 0$) also gives a very satisfactory analysis of the reduced HiPIP's susceptibility data, it appears that its success is first and foremost due to the importance of delocalization (as reflected by the optimal values of B), which leads to a probed electronic structure that can be described, simply, by a single parameter, J.

While so high optimal B values actually allow to ensure that the probed electronic structure consists of the three electronic levels $\mathcal{S}(S_{12} = {}^9/_2, S_{34} = {}^9/_2, S = 0, 1, 2; --)$ as the only thermally accessible levels in the experimentally available temperature range of 0−300 K (Figure 5), it can however be shown that this practically remains so for lower B values, that is, for $B < 1400$ cm^{-1}. First we note that B must be of the order of $2J$ for the influence of the degenerated triplets $\mathcal{S}(S_{12} = {}^9/_2, S_{34} = {}^7/_2, 1; --)$ and $\mathcal{S}(S_{12} = {}^7/_2, S_{34} = {}^9/_2, 1; --)$ located at $J + B$ to be able to compare with the influence of the quintet level at $3J$, the ratios of their populations and of their contributions to the molar susceptibility law (eq 5) being $\rho_{pop} = {}^5/_6 \exp[(B - 2J)/k_BT]$ and $\rho_{susc} = {}^5/_2 \exp[(B - 2J)/k_BT]$, respectively. When one then considers Figure 4, one notes that, with decreasing B values, n and J differ from their optimal values from 1100 cm^{-1} on only, as opposed to 1400 cm^{-1} for the residual. In addition a B value of 800 cm^{-1} is needed to observe a decrease of 0.02 μmol, that is, of twice the n-grid size, in the value of the critical n parameter.[60] For such a comparatively low value, (i) the changes in J and $\mathcal{R}$ are only of −5 cm^{-1} and +0.07 respectively, whereas (ii) the ratios ρ_{pop} and ρ_{susc} stay in favor of the quintet state for usual temperatures. Thus the description of the electronic structure which has been deduced from the optimal solutions is preserved for suboptimal B values. This observation is also emphasized by Table 1B, which lists residual and parameter values of fit results which have been obtained for these B values and for which the amount of proteins differs from the optimal n value by at most 0.02 μmol (see also Figure 4). The large uncertainty on the B value may mainly be explained by the fact that the temperature range used to probe the electronic structure was actually too small to allow a significant population of states whose energies depend on the B parameter (e.g., the degenerated triples $\mathcal{S}(S_{12} = {}^9/_2, S_{34} = {}^7/_2, 1; --)$ and $\mathcal{S}(S_{12} = {}^7/_2, S_{34} = {}^9/_2, 1; --)$ located at $J + B$ above the ground state).

Finally, the critical study of the magnetization data of the reduced HiPIP of *C. vinosum* within the exchange and double exchange theoretical framework has resulted in a reliable quantitative description of its electronic structure. It however does not allow us to propose a definitive value for the double exchange parameter B. This issue will be addressed later on through the analysis of the reported 77 K absorption spectrum of the protein.[64]

(64) Cerdonio, M.; Wang, R.-H.; Rawlings, J.; Gray, H. B. *J. Am. Chem. Soc.* **1974**, *96*, 6534−6535.

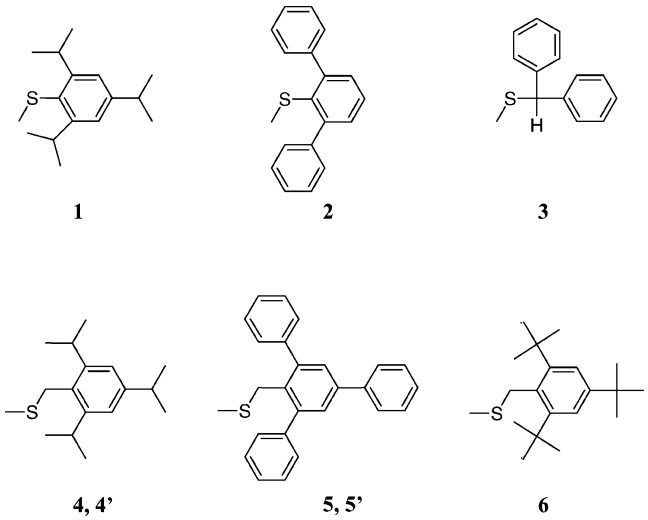

Figure 6. Recapitulative scheme of the ligands used in the model compounds $(Cat)_2[Fe_4S_4(SR)_4]$, where $RS^- = $ 2,4,6-triisopropylphenylthiolate (**1**), 2,6-diphenylphenylthiolate (**2**), diphenylmethylthiolate (**3**), 2,4,6-triisopropylbenzylthiolate (**4**, **4′**), 2,4,6-triphenylbenzylthiolate (**5**, **5′**), 2,4,6-tri-*tert*-butylbenzylthiolate (**6**), and where Cat = NEt_4 (**1**, **2**, **3**, **4′**, **5′**, **6**), PPh_4 (**4**, **5**).

Studies of HiPIP Relevant Model Compounds in the $[Fe_4S_4]^{2+}$ Oxidation State. Figure 6 recapitulates the ligands used in the HiPIP relevant model compounds and the notations used to designate them.

1. X-ray Study of the Novel $(NEt_4)_2[Fe_4S_4(S\text{-}2,6\text{-}(Ph)_2C_6H_3)_4]$ Compound. Formulation of **2** was confirmed by the X-ray study. A stereoscopic view of the $[Fe_4S_4(S\text{-}2,6\text{-}(Ph)_2C_6H_3)_4]^{2-}$ anion is given in Figure 7. The cubane-type $[Fe_4S_4]$ core is remarkably capped by the ligands' phenyl rings. The high degree of covering offered by the aromatic rings appears to be promoted by the pronounced noncoplanarity of the aromatic substituent rings pertaining to a same ligand. If one considers the dihedral angle characterizing this deviation, one notes that the phenyl substituents of a given ligand are not equivalent, the dihedral angle being significantly more important for one substituent than for the other (63.6−77.7° vs 52.7−57.1°). Moreover, the values of both types of dihedral angles vary from one ligand to another, indicating that there is no symmetry imposed on the $[Fe_4S_4(S\text{-}2,6\text{-}(Ph)_2C_6H_3)_4]^{2-}$ anion. Selected distances and angles are presented in Table 2. Inspection of Table 2 confirms the absence of molecular symmetry, even at the $[Fe_4S_4(SC)_4]$ unit level. Nevertheless, the $[Fe_4S_4]$ core approaches D_{2d} symmetry with a (noncrystallographically imposed) S_4 axis through the upper and lower faces of the polyhedron, as shown in Figure 1. Under the assumed D_{2d} symmetry, distance and angle sets characterizing the core structure divide into two sets, presented in Table 2. In particular, four shorter Fe−μ_3-S bonds (average distance, 2.263 Å) and eight longer Fe−μ_3-S bonds (average distance 2.300 Å), which are respectively approximately parallel and perpendicular to the idealized S_4 axis, characterize the tetragonal compression of the core along this idealized symmetry axis. Table 3 lists mean values of selected distances and angles in $\mathbf{2}^{2-}$ and in other $[Fe_4S_4]^{2+}$ complexes. Comparison of the structural parameters shows that the distortion of the $\mathbf{2}^{2-}$ $[Fe_4S_4]$ core fits

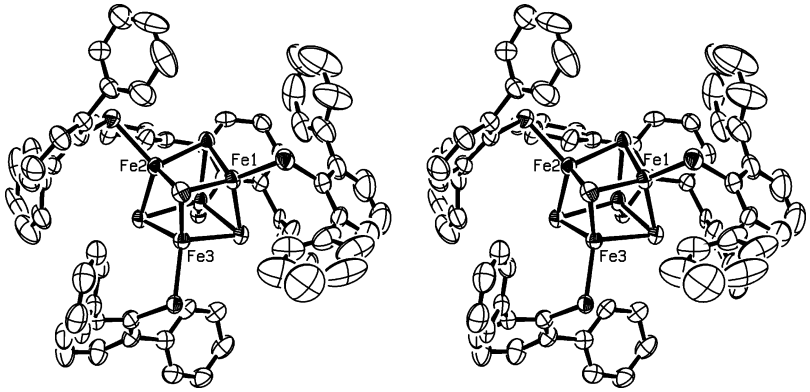

Figure 7. An ORTEP[81] stereoscopic view of the $[Fe_4S_4(S\text{-}2,6\text{-}(Ph)_2C_6H_3)_4]^{2-}$ anion, complete except for hydrogen atoms (the 50% probability ellipsoids are shown).

Table 2. Selected Distances (Å) and Angles (deg) Characterizing the Structure of the $[Fe_4S_4(S\text{-}2,6\text{-}(Ph)_2C_6H_3)_4]^{2-}$ Anion[a]

Fe−Fe		*mean*	2.287
Fe_1-Fe_2	2.7770(17)	Fe−S*−Fe	
Fe_3-Fe_4	2.7328(16)	$Fe_1-S_1-Fe_2$	74.01(8)
mean	*2.7549*	$Fe_1-S_2-Fe_2$	74.20(8)
Fe_1-Fe_3	2.7615(17)	$Fe_3-S_3-Fe_4$	73.02(7)
Fe_1-Fe_4	2.7700(17)	$Fe_3-S_4-Fe_4$	73.11(8)
Fe_2-Fe_3	2.7604(17)	*mean*	*73.59*
Fe_2-Fe_4	2.7547(16)	$Fe_1-S_1-Fe_3$	73.76(8)
mean	*2.7617*	$Fe_2-S_1-Fe_3$	74.21(8)
mean (of 6)	*2.7594*	$Fe_1-S_2-Fe_4$	75.05(8)
Fe−S*		$Fe_2-S_2-Fe_4$	74.11(8)
Fe_1-S_3	2.253(2)	$Fe_1-S_3-Fe_3$	74.49(8)
Fe_2-S_4	2.259(3)	$Fe_1-S_3-Fe_4$	75.25(8)
Fe_3-S_1	2.281(3)	$Fe_2-S_4-Fe_3$	75.03(8)
Fe_4-S_2	2.257(3)	$Fe_2-S_4-Fe_4$	74.08(8)
mean	*2.263*	*mean*	*74.49*
Fe_1-S_1	2.320(2)	*mean (of 12)*	*74.19*
Fe_1-S_2	2.290(3)	S−C(ring)	
Fe_2-S_1	2.294(3)	S_5-C_1	1.769(10)
Fe_2-S_2	2.314(2)	S_6-C_{21}	1.764(9)
Fe_3-S_3	2.309(2)	S_7-C_{41}	1.786(9)
Fe_3-S_4	2.274(2)	S_8-C_{61}	1.761(8)
Fe_4-S_3	2.284(2)	*mean*	*1.770*
Fe_4-S_4	2.314(2)	Fe−S−C(ring)	
mean	*2.300*	$Fe_1-S_5-C_1$	101.9(3)
Fe−S		$Fe_2-S_6-C_{21}$	99.5(3)
Fe_1-S_5	2.286(3)	$Fe_3-S_7-C_{41}$	107.7(3)
Fe_2-S_6	2.278(3)	$Fe_4-S_8-C_{61}$	104.6(3)
Fe_3-S_7	2.290(3)	*mean*	*103.4*
Fe_4-S_8	2.295(2)		

[a] Bridging μ_3-S atoms are noted S*.

Table 3. Comparison of Mean Values of Selected Distances (Å) and Angles (deg) in $[Fe_4X_4]^{2+}$ (X = S, Se) Complexes[a]

	$[Fe_4S_4(S\text{-}2,6\text{-}(Ph)_2C_6H_3)_4]^{2-}$ [b]	$[Fe_4S_4(SC_6H_5)_4]^{2-}$ [c]
Fe−Fe	2.7549 (2), 2.7617 (4)	2.730 (2), 2.739 (4)
Fe−S*	2.263 (4), 2.300 (8)	2.267 (4), 2.296 (8)
Fe−S*−Fe	74.19	73.50
Fe−S	2.287	2.263
S−C(ring)	1.770	1.771
Fe−S−C(ring)	103.4	106.1
	$[Fe_4S_4(SCH_2C_6H_5)_4]^{2-}$ [d]	$[Fe_4S_4(S\text{-}t\text{-}Bu)_4]^{2-}$ [e]
Fe−Fe	2.776 (2), 2.732 (4)	2.749 (2), 2.764 (4)
Fe−S*	2.239 (4), 2.310 (8)	2.274 (4), 2.294 (8)
Fe−S*−Fe	73.8	74.1
Fe−S	2.251	2.254
	$[Fe_4Se_4(S\text{-}t\text{-}Bu)_4]^{2-}$ [f]	*C. vinosum* HiPIP[g]
Fe−Fe	2.817 (2), 2.812 (4)	2.744 (2), 2.708 (4)
Fe−X*	2.274 (4), 2.417(8)	2.249 (4) 2.307 (8)
Fe−S	2.248	2.272

[a] The symbol X* refers to bridging μ_3-X (X = S, Se) atoms. The number of averaged values is given when two distances are given. [b] This work. [c] Me_4N^+ salt.[65] [d] Et_4N^+ salt.[79] [e] Et_4N^+ salt; real D_{2d} site symmetry.[47] [f] Et_4N^+ salt.[63] [g] Reference 87.

well with the trend observed for biological or synthetic $[Fe_4S_4]^{2+}$ clusters, namely, a compressed D_{2d} type distortion of the core. The differences in the core structure of these complexes are small as emphasized by a comparison between $\mathbf{2}^{2-}$ and notably the parent non diphenyl substituted dianion $[Fe_4S_4(SC_6H_5)_4]^{2-}$.[65] These small differences are especially illustrative of the known fact[47] that the modification of the chemical environment of the $[Fe_4S_4]^{2+}$ core does not have a drastic influence on its structure. Concerning the relative positions of the ligands in both anions, a small lengthening of the Fe−S distance is observed when going from $[Fe_4S_4(SC_6H_5)_4]^{2-}$ to $\mathbf{2}^{2-}$, which is probably due to the more important bulkiness of the $\mathbf{2}^{2-}$ ligands. In parallel, there is a decrease of the Fe−S−C(ring) angles which may be related to the way in which the ligands of $\mathbf{2}^{2-}$ cap the $[Fe_4S_4]^{2+}$ cluster: both packing forces and van der Waals interactions (between the aromatic rings and the $[Fe_4S_4]^{2+}$ cluster) are likely to play an important role in the final positioning of the aromatic rings. Such a positioning may well persist in solution, since room temperature ^{1}H NMR studies give short T_1 relaxation times which are indicative of a close vicinity between the rings and the core (see text below and Table 5).

2. Redox Properties. The redox properties of the $[Fe_4S_4]^{2+}$ dianions $\mathbf{2}^{2-}$, $\mathbf{3}^{2-}$, $\mathbf{5}^{2-}$, and $\mathbf{6}^{2-}$ have been investigated by cyclic voltammetry in CH_2Cl_2. The results are summarized and compared in Table 4 to the ones previously reported for $\mathbf{1}^{2-}$ and $\mathbf{4}^{2-}$.[15,18] A reversible or pseudoreversible one-electron oxidation process is observed for all compounds. Nevertheless $\mathbf{2}^{2-}$ shows, in addition to the oxidation process present at $E_{1/2} = +15$ mV vs NHE, a second oxidation process at $E_{1/2} = +210$ mV vs NHE ($\Delta E = 100$ mV). Further studies revealed that this redox phenomenon possesses the following characteristics: (i) both oxidation processes are one-electron processes leading to the oxidized compound since the electrolysis of the solution at +560 mV vs NHE gives the $[Fe_4S_4]^{3+}$ species; (ii) the relative intensity of the waves

(65) Que, L., Jr.; Bobrik, M. A.; Ibers, J. A.; Holm, R. H. *J. Am. Chem. Soc.* **1974**, *96*, 4168−4178.

Table 4. Redox Properties of a Selection of HiPIP Relevant Model Compounds[a]

	$[Fe_4S_4]^{3+/2+}$ $E_{1/2}$ [ΔE]	$[Fe_4S_4]^{2+/+}$ $E_{1/2}$ [ΔE]
$[Fe_4S_4(S\text{-}2,4,6\text{-}(i\text{-}Pr)_3C_6H_2)_4]^{2-}$ ($\mathbf{1}^{2-}$)[15]	+125 (r)[b]	−955 (pr)
$[Fe_4S_4(S\text{-}2,6\text{-}(Ph)_2C_6H_3)_4]^{2-}$ ($\mathbf{2}^{2-}$)	+15 [100] (pr) [b,c]	
$[Fe_4S_4(SCH(Ph)_2)_4]^{2-}$ ($\mathbf{3}^{2-}$)	+304 [74] (r)	−875 [150] (pr)
$[Fe_4S_4(SCH_2\text{-}2,4,6\text{-}(i\text{-}Pr)_3C_6H_3)_4]^{2-}$ ($\mathbf{4}^{2-}$)[18]	+64 [150] (pr)	−755 (ir)[d]
$[Fe_4S_4(SCH_2\text{-}2,4,6\text{-}(Ph)_3C_6H_2)_4]^{2-}$ ($\mathbf{5}^{2-}$)	+140 [180] (pr) [b]	
$[Fe_4S_4(SCH_2\text{-}2,4,6\text{-}(t\text{-}Bu)_3C_6H_2)_4]^{2-}$ ($\mathbf{6}^{2-}$)	+117 [152] (pr) [b]	−1198 [196] (pr)

[a] The $E_{1/2}$ (mV vs NHE) and ΔE (mV) values result from cyclic voltammetry studies in CH_2Cl_2. The designations r, pr, and ir indicate reversible ($\Delta E \sim 60$ mV), pseudoreversible ($\Delta E \geq 100$ mV), and irreversible redox processes, respectively. [b] The oxidized $[Fe_4S_4]^{3+}$ species have been isolated in the solid state. [c] A second oxidation process is observed at +210 mV vs NHE (see text). [d] The reported irreversible reduction is observed in CH_3CN.

Table 5. Proton NMR Shifts δ (ppm) and Relaxation Times T_1 (ms) Determined at 293 K for Compounds **1**,[67] **2**, **3**, **4′**,[18] **5′**, and **6**[a]

	δ (ppm)	T_1 (ms)
	$(NEt_4)_2[Fe_4S_4(S\text{-}2,4,6\text{-}(i\text{-}Pr)_3C_6H_2)_4]$ (**1**)[b]	
m-H	8.06 [7.05]	70
o-CH	4.84 [3.55]	4
o-CH_3	1.47 [1.30]	29
p-CH	3.17 [2.91]	184
p-CH_3	1.24 [1.29]	247
	$(NEt_4)_2[Fe_4S_4(S\text{-}2,6\text{-}(Ph)_2C_6H_3)_4]$ (**2**)[b]	
m-H	8.25 [7.30−7.40]	59
p-H	6.29 [7.30−7.40]	96
m′-H	7.80 [7.30−7.40]	7
o′, *p′*-H	7.30 [7.30−7.40]	28
	$(NEt_4)_2[Fe_4S_4(SCH(Ph)_2)_4]$ (**3**)[c]	
−CH−	11.30 [5.40]	2.4
m-H	7.60 [7.20−7.50]	14
o-H	7.45 [7.20−7.50]	80
p-H	7.00 [7.20−7.50]	131
	$(NEt_4)_2[Fe_4S_4(SCH_2\text{-}2,4,6\text{-}(i\text{-}Pr)_3C_6H_3)_4]$ (**4′**)[c]	
$-CH_2-$	14.40 [3.81]	3.5
m-H	7.20 [7.00]	138[d]
o-CH	3.80 [3.23]	8[d]
o-CH_3	1.46 [1.24]	47[d]
p-CH	3.00 [2.84]	347[d]
p-CH_3	1.30 [1.24]	300[d]
	$(NEt_4)_2[Fe_4S_4(SCH_2\text{-}2,4,6\text{-}(Ph)_3C_6H_2)_4]$ (**5′**)[c]	
$-CH_2-$	13.80 [3.63]	3.2
H (aromatic)	7.20−7.80 [7.30−7.60]	
	$(NEt_4)_2[Fe_4S_4(SCH_2\text{-}2,4,6\text{-}(t\text{-}Bu)_3C_6H_2)_4]$ (**6**)[c]	
$-CH_2-$	15.70 [4.34[e]]	2
m-H	7.50 [7.33[e]]	110
o-*t*-Bu	1.90 [1.50[e]]	21
p-*t*-Bu	1.30 [1.33[e]]	277

[a] NMR shift values given in brackets are those obtained for the free ligands. [b] Measurements were performed in CD_3CN. [c] Measurements were performed in CD_2Cl_2. [d] Determined in CD_3CN. [e] Determined in $CDCl_3$.

associated with both processes varies according to the experimental conditions (in particular, it depends on the Pt electrode used as working electrode). These characteristics allow an explanation of the existence of the two processes by a heterogeneous behavior of the $\mathbf{2}^{2-}$ compound at the Pt electrode's surface. Such a hypothesis is reinforced by the fact that the one-electron reduction of the isolated oxidized $\mathbf{2}^{-}$ anion occurs in a single-step process corresponding to the one located at the lowest potential.

Except for the compounds with diphenylmethylthiolate and 2,4,6-triisopropylbenzylthiolate ligands, all oxidized compounds are stable in CH_2Cl_2 solvent and could thus be isolated in the solid state after chemical oxidation of the reduced species.[19,20] Even though the oxidized compounds $[Fe_4S_4(SCH(Ph)_2)_4]^{-}$ and $[Fe_4S_4(SCH_2\text{-}2,4,6\text{-}(i\text{-}Pr)_3C_6H_3)_4]^{-}$ could not be isolated in the solid state, they can be stabilized in solution by the bulky diphenylmethylthiolate and 2,4,6-triisopropylbenzylthiolate ligands. The two compounds were generated in situ and could be studied by NMR and EPR spectroscopies. These studies indicated that the eventual degradation, in both cases, proceeds through a $[Fe_3S_4]^{+}$ intermediate.[18,19]

A pseudoreversible one-electron reduction process is observed for the $\mathbf{1}^{2-}$, $\mathbf{3}^{2-}$, and $\mathbf{6}^{2-}$ compounds in CH_2Cl_2. In the case of the $\mathbf{4}^{2-}$compound, only an irreversible reduction could be observed in CH_3CN. No reduction is observed in the case of the $\mathbf{2}^{2-}$ and $\mathbf{5}^{2-}$ compounds. It is interesting to note that these compounds are the ones possessing the highest number of phenyl rings surrounding the $[Fe_4S_4]$ core.

3. Magnetization Studies. Figure 2 summarizes the magnetization data recorded on compounds **1**−**6**. Data are displayed as the product of the experimental molar susceptibility χ_{exp} by temperature plotted against temperature. The shapes of the curves are similar to those observed in the case of the reduced HiPIP, and express the existence of antiferromagnetic coupling within the systems. Below a critical temperature, varying between 65 and 90 K according to the compounds, the behavior of the curves indicates the population of diamagnetic state(s). The nonzero values of $\chi_{exp}T$ and, in some cases, the observed decrease on cooling indicate the presence in weak amounts of high-spin ferric impurities ($S = {}^5/_2$) with anisotropy, as confirmed through EPR controls. The increase of $\chi_{exp}T$ observed above the critical temperatures indicates that population of excited paramagnetic states occurs when the temperature is raised. Concerning compounds **2**, **5**, and **6**, some experimental points above 45 K, represented by open symbols, deviate from the ideal curves expected for these compounds. These artifacts are due to the random entry of small amounts of oxygen in the Quantum Design magnetometer at lowest temperatures and to its evaporation above 45 K. Data affected by this phenomenon were not taken into account during the fitting procedure, done within the exchange and double exchange theoretical framework, using eq 2. ΔJ was also set to zero after its correlation with the parameter B was noticed. Error maps, constructed by letting vary the amount n of $[Fe_4S_4]^{2+}$ complex and $B = B_{\Delta J=0}$ with increments of 0.01 mol and 100 cm^{-1}, are displayed in Figure 8. The surfaces present real minima in the case of compounds **1**, **3**, and **4**, and valleys that are narrow along the n direction and large along the B direction in the case of compounds **2**, **5**, and **6**. Characteristics of these regions are illustrated by Figure 4, which gives the plots against B of the best values obtained at fixed B's for the residual and the n parameter, as well as for the J parameter. The $\mathscr{R}$ curves of Figure 4 show that the three true minima are flat in the direction of increasing B values although the well depth is relatively greater in the case of compound **3** than for **1** and **4**. As for the n curves, the fact that they vary little and quite slowly illustrates the narrowness along the n direction of the map regions of smallest $\mathscr{R}$ values. The similitude observed in Figure 4 between the n and J curves

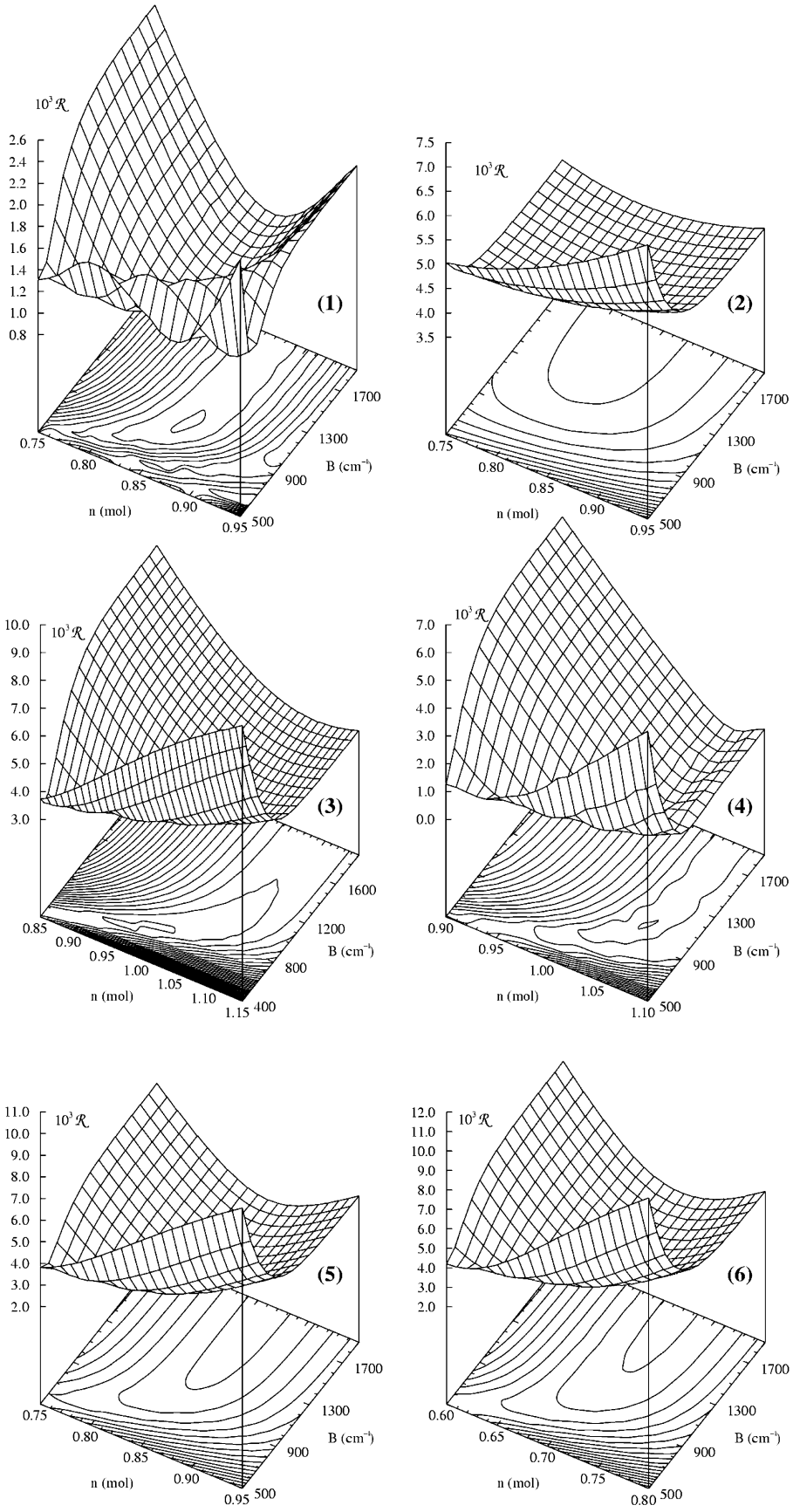

Figure 8. Error maps constructed by fitting the magnetization data of compounds **1**−**6** for fixed values of *n* and *B* (with ΔJ kept fixed to zero).

is due to the positive correlation between both parameters that was already mentioned in the study of the magnetization data of the reduced HiPIP. The optimal *n*, *J*, and *B* parameter values defined by the minima and valleys are summarized

in Table 1A. One thus notes that the determined amounts *n* of $[Fe_4S_4]^{2+}$ complexes are as expected close to the theoretical value of 1 mol. The lines represented in Figure 2 correspond to the χT curves generated by the optimal parameter values. In all cases, a very satisfactory agreement was obtained between the experimental data and the theoretical curves. The quality of the fits is confirmed by the small values of the residual given in Table 1A.

The electronic structures of the model compounds are characterized by optimal *J* values which vary between 261(2) and 397(8) cm^{-1} depending on the compounds and, whatever the compound, by high optimal *B* values (Table 1A). The important gain of delocalization energy is, as in the case of the reduced HiPIP from *C. vinosum*, responsible for the stabilization of the three lowest lying levels $\mathcal{E}(S_{12} = {}^9/_2, S_{34} = {}^9/_2, S; --)$, $S \in \{0, 1, 2\}$. These levels are the only significantly populated levels within the temperature range used for the experiments, and their energy gaps follow the Landé rule. For compound **3**, the set of significantly populated levels actually reduces to the $S = \{0, 1\}$ levels because of the large *J* value (397(8) cm^{-1}) which puts the quintet state high in energy. Remarkably the representations we have obtained for the thermally accessible electronic levels of the $[Fe_4S_4]^{2+}$ complexes are retained for nonoptimal *B* values, explaining the flatness in the *B* direction of the map regions of smallest $\mathcal{R}$ values. Such *B* values are given in Table 1B. They have been selected as they lead to fit results with values of the critical *n* parameter which differ from the optimum *n* values by at most ± 0.02 mol, that is twice the *n*-grid size. One can thus see in Table 1B that the *J* and $\mathcal{R}$ values associated with these results remain quite close to their optimal values despite significant differences between optimal and nonoptimal *B*'s. Such an uncertainty on the *B* values may be explained, as in the case of the reduced HiPIP, by a probe temperature range which is too small to allow the significant thermal population of electronic levels whose energies depend on the *B* parameter.

With compound **3**, this uncertainty issue apparently does not arise given that the above selection criterion is such that one stays trapped in the observed minimum, that is, with *B* in the 500−700 cm^{-1} range, although it should be noted that the set of significantly populated levels $\mathcal{E}(S_{12} = {}^9/_2, S_{34} = {}^9/_2, S; --)$, $S = \{0, 1\}$, clearly remains the same for $B \geq 700$ cm^{-1}. When one then considers for $J = 397(8)$ cm^{-1} and $B = 600(100)$ cm^{-1} the excited levels that come just after the first excited state, one notes that there are levels whose energies depend on *B*. They are the degenerated triples $\mathcal{E}(S_{12} = {}^9/_2, S_{34} = {}^7/_2, 1; --)$ and $\mathcal{E}(S_{12} = {}^7/_2, S_{34} = {}^9/_2, 1; --)$ which are at $J + B = 1097(101)$ cm^{-1}; they lie below the quintet $\mathcal{E}(S_{12} = {}^9/_2, S_{34} = {}^9/_2, 2; --)$ which is at $3J = 1191(14)$ cm^{-1} above the ground level, at approximatively the same energy as the single $\mathcal{E}(S_{12} = {}^7/_2, S_{34} = {}^7/_2, 0; --)$ located at $2B = 1200(142)$ cm^{-1}. Hence, despite the fact that for the highest probe temperature of 300 K the populations of the triples (3.2%), quintet (1.1%), and single (0.2%) remain weak (particularly with regard to the populations of the ground (66.2%) and first excited (29.2%) states), it is likely that, thanks to the high sensitivity of SQUID magnetometers, the slight population at high temperatures of the degenerated triples and maybe of the single allowed a precise determination of *B*. However, it might also be that a *B* value of 600(100) cm^{-1} simply puts the triples and single at places that allow them to optimally act like substitutes for the vibrational levels of the compound's ground and first excited electronic states which are not accounted for in eq 5. Indeed the thermal population of the triples and single translates into a diminishing of the paramagnetic contribution of the quintet which in reality could be due to the population of these vibrational levels.[66]

Thus, while a reliable quantitative description of the electronic structures of the model compounds has been achieved from the exchange and double exchange treatment of their magnetization data, further investigations are in fact required to determine definitive double exchange parameter values. Variable temperature optical studies proved to be adequate for this purpose.

4. Proton NMR Studies. ^{1}H NMR studies were performed at 293 K on the model compounds **2**, **3**, **5′**, and **6**. Figure 9 shows the 293 K ^{1}H NMR spectra of $(NEt_4)_2[Fe_4S_4(SCH\text{-}(Ph)_2)_4]$ (**3**) in CD_3CN, of $(NEt_4)_2[Fe_4S_4(SCH_2\text{-}2,4,6\text{-}(Ph)_3C_6H_2)_4]$ (**5′**), and of $(NEt_4)_2[Fe_4S_4(SCH_2\text{-}2,4,6\text{-}(t\text{-}Bu)_3C_6H_2)_4]$ (**6**) in CD_2Cl_2. The chemical shifts and the relaxation times T_1 determined for the newly synthesized compounds, as well as those previously reported for compounds **1**[67] and **4′**,[18] are given in Table 5.

The differences between the chemical shifts of free and coordinated ligands (Table 5) account for the paramagnetism arising from the population of the triplet $\mathcal{E}(S_{12} = {}^9/_2, S_{34} = {}^9/_2, 1; --)$ and quintet $\mathcal{E}(S_{12} = {}^9/_2, S_{34} = {}^9/_2, 2; --)$ excited states. They correspond to hyperfine contributions which are predominantly scalar in nature. Thus, for the newly synthesized complexes, the proton resonances are hardly affected by the coordination, except for the SCH protons of compound **3** and the SCH_2 protons of compounds **5′** and **6**, which are only three bond distant from the clusters. With observed downfield hyperfine shifts of the order of 10 ppm, the resonance values of these latter protons (11.30, 13.80, and 15.70 ppm respectively for SCH in **3**, SCH_2 in **5′** and in **6**)

(66) For compound **3**, the slight increase of the $\mathcal{R}$ curve of Figure 4 when *B* is augmented from 600 cm^{-1} on is due to the fact that the weak paramagnetic influence of the quintet $\mathcal{E}(S_{12} = {}^9/_2, S_{34} = {}^9/_2, 2; --)$ becomes less and less attenuated by the presence of the degenerated triples $\mathcal{E}(S_{12} = {}^9/_2, S_{34} = {}^7/_2, 1; --)$ and $\mathcal{E}(S_{12} = {}^7/_2, S_{34} = {}^9/_2, 1; --)$ and single $\mathcal{E}(S_{12} = {}^7/_2, S_{34} = {}^7/_2, 0; --)$. Indeed, these latter states, located at $J + B$ and $2B$, respectively, get rejected higher in energy so that the quintet only can be populated at high temperatures. This illustrates this possible moderating role of the triples and single we are talking about. Let us also indicate that the increase of the *J* curve of Figure 4 is also indicative of the need to reduce the contribution of this quintet located at $3J$ to the paramagnetic properties. However, the *J* parameter being primarily determined by the temperature at which the first excited state $\mathcal{E}(S_{12} = {}^9/_2, S_{34} = {}^9/_2, 1; --)$ located at *J* becomes significantly populated, the extent to which *J* can depart from its optimal *J* value is quite limited: we can deduce from the *J* curve that this increase is of at most $+25$ cm^{-1}.

(67) Tsan, P. ENSCP training course, 1993.

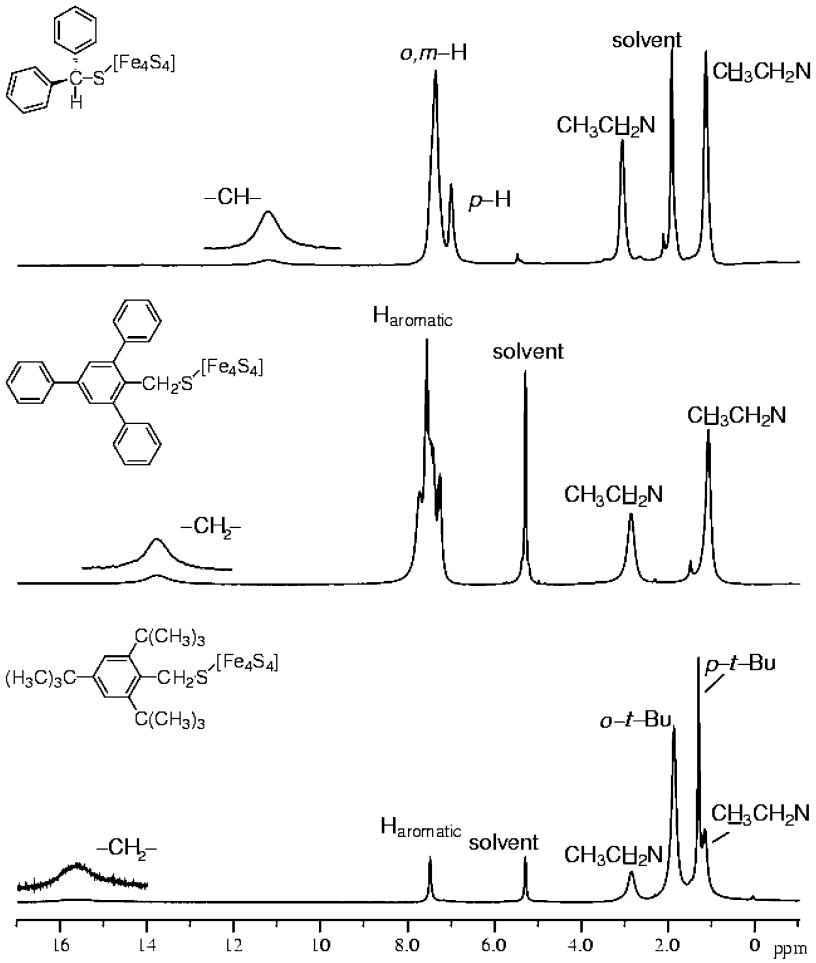

Figure 9. ^{1}H NMR spectra, at 293 K, of $(NEt_4)_2[Fe_4S_4(SCH(Ph)_2)_4]$ in CD_3CN (top) and of $(NEt_4)_2[Fe_4S_4(SCH_2\text{-}2,4,6\text{-}(Ph)_3C_6H_2)_4]$ (middle) and $(NEt_4)_2[Fe_4S_4(SCH_2\text{-}2,4,6\text{-}(t\text{-}Bu)_3C_6H_2)_4]$ (bottom) in CD_2Cl_2.

are close to those found for the SCH_2 protons in $[Fe_4S_4(SEt)_4]^{2-}$ (12.5 ppm at 295 K, in CD_3CN),[68] $[Fe_4S_4(SCH_2CH_2OH)_4]^{2-}$ (12.9 ppm at 307 K, in $S(CD_3)_2O$),[34] $[Fe_4S_4(SCH_2Ph)_4]^{2-}$ (13.8 ppm at 295 K, in $CDCN_3$),[68] and $[Fe_4S_4(SCH_2\text{-}2,4,6\text{-}(i\text{-}Pr)_3C_6H_3)_4]^{2-}$ (14.4 ppm at 293 K, in CD_2Cl_2).[18]

The relaxation properties of the ligands' protons are also affected by the paramagnetism of the cluster, as evidenced by the very short T_1 values (Table 5), and, for **3**, **5′**, and **6**, also by the broad signals due to the SCH and SCH_2 protons (Figure 9), which account for a shortening of the T_2 transverse relaxation times. The relaxation mechanism is mainly dipolar, and, for a given compound, T_1 depends on the distance between the paramagnetic center and the considered protons. T_1 values obtained for compounds **1** and **2**, indeed, appear in increasing order for protons located (or pertaining to a substituent located) at ortho, meta, and para positions of the main phenyl groups. This order corresponds to increasing distance of the protons from the paramagnetic center when going successively from ortho to meta and finally to para positions. For compounds **3**, **4**, **5′**, and **6**, the shortest T_1 values are obtained for the SCH or SCH_2 protons. T_1 then progressively increases for protons located (or belonging to substituents located) at ortho, meta, and para positions of the main phenyl group of the ligands. As for compounds **1** and **2**, the increase of the T_1 values corresponds to moving away from the paramagnetic centers. Similarly, the different T_1 values observed for protons belonging to the same substituent (*o*-*i*-Pr or *p*-*i*-Pr for compounds **1** and **4**, *o*-Ph for compound **2**) reflect the differences in their proximity to the compound's $[Fe_4S_4]$ core.

The temperature dependence of the SCH_2 proton resonance of compounds **5′** and **6** has also been studied. The results are shown in Figure 10A along with those obtained for **4′** (which were briefly described elsewhere[18]). The observed anti-Curie temperature dependence is similar to the one reported for similar methylene protons present in $[Fe_4S_4(SCH_2Ph)_4]^{2-}$,[68] in the reduced HiPIP from *C. vinosum*[69] and other $[Fe_4S_4]^{2+}$ proteins.[70] In order to simulate this behavior, we assume that the paramagnetic shift is due to the Fermi contact shift, and that protons pertaining to a given ligand only sense the paramagnetic site Fe_i (i = 1, ..., 4) coordinated by the

(68) Holm, R. H.; Phillips, W. D.; Averill, B. A.; Mayerle, J. J.; Herskovitz, T. *J. Am. Chem. Soc.* **1974**, *96*, 2109−2117.

(69) Bertini, I.; Briganti, F.; Luchinat, C.; Scozzafava, A.; Sola, M. *J. Am. Chem. Soc.* **1991**, *113*, 1237−1245.

(70) Bertini, I.; Ciurli, S.; Luchinat, C. In *Structure and Bonding*; Springer: Berlin, Heildeberg, 1995; Vol. 83 and references therein.

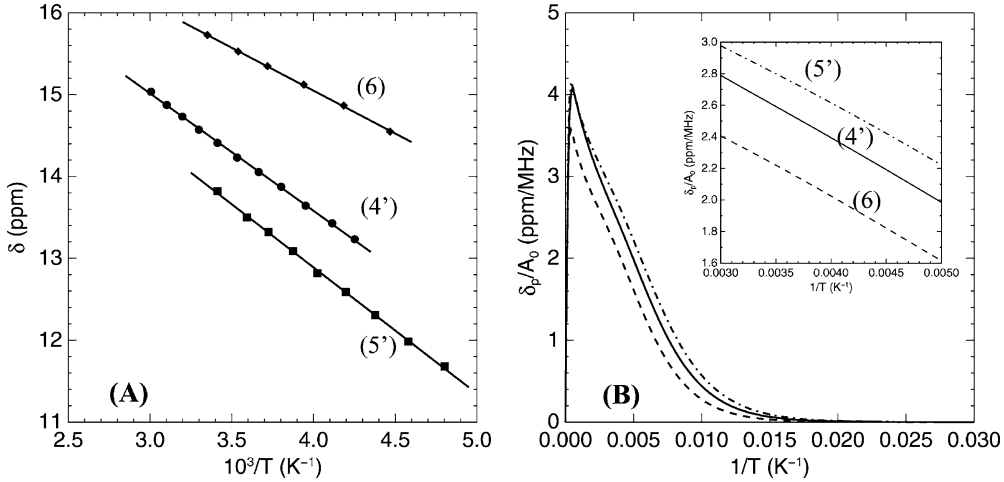

Figure 10. (A) Temperature dependence of the SCH_2 proton resonance of compounds **4′**, **5′**, and **6**. (B) Simulated temperature dependence of the paramagnetic shift of compounds **4′**, **5′**, and **6** using eq 9 with $A_0 = 1$ MHz, and the values of parameters J and B deduced from magnetization data (Table 1A); the inset emphasizes the theoretical curve behavior over the experimentally available temperature range (see text).

ligand. The paramagnetic contribution reads[70]

$$\delta_{p,i}(T) = \frac{g_e\mu_B}{g_H\mu_N} \times \frac{A_i}{3k_BT} \times \frac{\sum_n K_i(n)S_n(S_n+1)(2S_n+1)\exp(-E_n/k_BT)}{\sum_n (2S_n+1)\exp(-E_n/k_BT)} \quad (8)$$

where μ_N is the nuclear magnet and A_i is the intrinsic hyperfine coupling constant (when the iron sites are not coupled). The summations run over the system's spin levels characterized by the total spin S_n. $K_i(n)$ are projection coefficients given by

$$K_i(n) = \frac{\langle S_n|\vec{s}_i\cdot\vec{S}|S_n\rangle}{\langle S_n|\vec{S}\cdot\vec{S}|S_n\rangle}$$

where $\vec{s}_i$ and $\vec{S}$ are center i and total spin operators, respectively. Given the theoretical model used, the four iron sites are equivalent and the paramagnetic shifts $\delta_{p,i}(T)$ (i = 1, 2, 3, 4) are all equal; the index i can therefore be dropped. One can show[63] in the present case that δ_p is proportional to the molar susceptibility. To proceed, it is sufficient here to notice that $\forall n$, $1 = \sum_{i=1}^{4} K_i(n)$, and, using the relation $\delta_p = \sum_{i=1}^{4}\delta_{p,i}/4$, one obtains for δ_p the relation

$$\delta_p(T) = \frac{g_e\mu_B}{g_H\mu_N} \times \frac{A_0}{12k_BT} \times \frac{\sum_n S_n(S_n+1)(2S_n+1)\exp(-E_n/k_BT)}{\sum_n (2S_n+1)\exp(-E_n/k_BT)} \quad (9)$$

which shows its proportionality to χ_m (eq 5). The temperature dependence of the paramagnetic shift δ_p has been simulated for compounds **4′**, **5′**, and **6** using the values of parameters J and B deduced from the magnetization data of, respectively, compounds **4**, **5**, and **6** (Table 1A). Figure 10B shows the plots of δ_p vs $1/T$ calculated for the three synthetic analogues and for $A_0 = 1$ MHz. An anti-Curie temperature dependence is observed in the 235−330 K temperature range available for liquid NMR experiments (see the inset, Figure 10B). Estimates of the SCH_2 protons hyperfine coupling constants A_0 for compounds **4′**, **5′**, and **6** are then given by the ratios of the slopes of the experimental curves (Figure 10A) and those of the corresponding simulated segments (inset, Figure 10B). The values obtained for A_0 are 3.6, 4.2, and 2.7 MHz for compound **4′**, **5′**, and **6**, respectively (Table 6).

Table 6. Isotropic Hyperfine Coupling Constants A_0 of the SCH_2 Protons of Coordinating Cysteines and Coordinating Benzylthiolates[a]

	reduced *C. vinosum* HiPIP	**4′**	**5′**	**6**
Π_{exp} (ppm K)	−1495[b]	−1430	−1521	−1050
Π_{th} (ppm K MHz^{-1})	−355	−396	−366	−386
$A_0 = \Pi_{exp}/\Pi_{th}$ (MHz)	4.2	3.6	4.2	2.7

[a] Π_{exp} represents the slope of the linear plot of the experimental isotropic shifts vs $1/T$ (an average value is given in the case of the reduced HiPIP). Π_{th} Represents the slope of the linear plot of the paramagnetic shift (given by eq 9 with $A_0 = 1$ MHz) vs $1/T$ in the 235−330 K temperature range available for liquid NMR experiments. [b] Average value of the slopes of the experimental curves published by Bertini et al.[69]

5. Variable Temperature Optical Studies. The NIR and visible domain optical properties of compounds **1**, **2**, **4′**, **5′**, and **6** have been investigated using variable temperature absorption spectroscopy over the 10−300 K temperature range. For comparison purposes, we have also studied $(NEt_4)_2[Fe_4S_4(SCH_2C_6H_5)_4]$ and the isomorph $(NEt_4)_2[Fe_4S_4(S\text{-}t\text{-}Bu)_4]$ and $(NEt_4)_2[Fe_4Se_4(S\text{-}t\text{-}Bu)_4]$ compounds. The plot of the temperature dependent absorption spectra A_T in the 400−2500 nm range, and the plot of $\delta A(T) = A_T - A_{10}$ difference curves over the 800−2500 nm range, are shown in Figure 11 for compounds **1**, **2**, **4′**, **6**, $(NEt_4)_2[Fe_4S_4(S\text{-}t\text{-}Bu)_4]$, and $(NEt_4)_2[Fe_4Se_4(S\text{-}t\text{-}Bu)_4]$. The data have been corrected from the KBr and background contributions.[71] One first notices that the absorption spectra A_T of all these compounds are structured alike. They possess dominating broad absorption bands in the 400−800 nm region whose

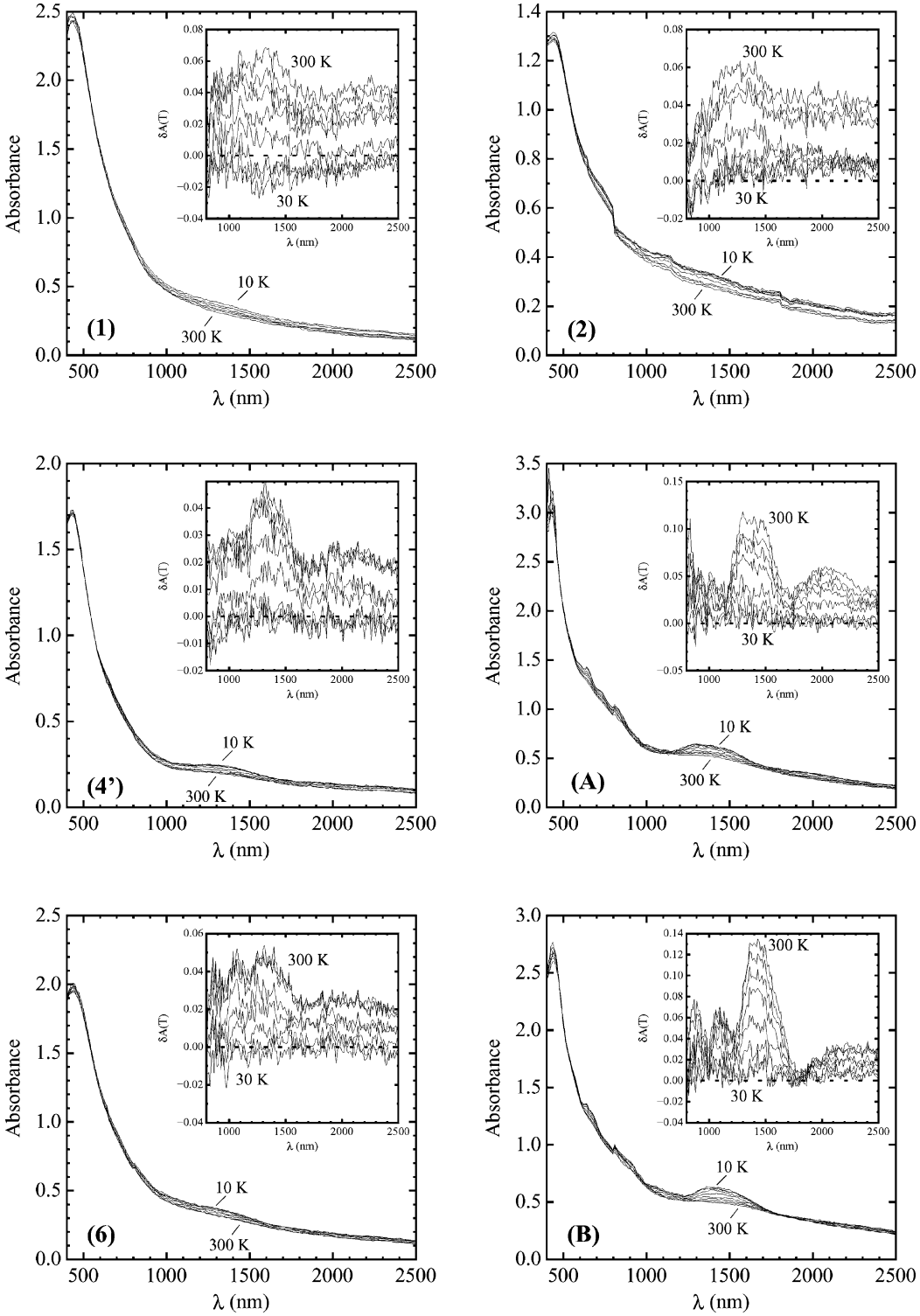

Figure 11. Temperature dependence of the absorption spectra of compounds **1**, **2**, **4′**, **6**, $(NEt_4)_2[Fe_4S_4(S\text{-}t\text{-}Bu)_4]$ (A), and $(NEt_4)_2[Fe_4Se_4(S\text{-}t\text{-}Bu)_4]$ (B) in the visible and NIR region between 10 and 300 *K*. Insets give the plot of the $\delta A(T) = A_{10} - A_T$ difference curves.

features are not well resolved: indeed, in addition to the most intense band whose maximum varies within the 430−440 nm region depending on the compound, one can guess the existence of at least a second transition at wavelengths greater than ∼550 nm. The most intense band is indicative of the presence of the $[Fe_4X_4]^{2+}$ (X = S, Se) core and of its coordination by thiolate ligands; it is assigned to X→Fe charge transfer transitions involving the bridging X^{2-} (X = S, Se) ions and the terminal ligands.[10,18,51,72,73] Inspection of

(71) Despite these corrections, it is still possible to observe vestiges of disruptions present in the compounds' raw data and also already pointed out in the KBr spectra (Figure S1). Their persistence may be due to the fact that the corrections cannot account for the variation with the samples of the sensitivity of the measurement setup (this one being tuned automatically).

(72) DePamphilis, B. V.; Averill, B. A.; Herskovitz, T.; Que, L., Jr.; Holm, R. H. *J. Am. Chem. Soc* **1974**, *96*, 4159−4167.

Table 7. Optical Properties of Compounds **1**, **2**, **4′**, **5′**, **6**, $(NEt_4)_2[Fe_4S_4(SCH_2C_6H_5)_4]$ (**A**), $(NEt_4)_2[Fe_4S_4(S\text{-}t\text{-}Bu)_4]$ (**B**), and $(NEt_4)_2[Fe_4Se_4(S\text{-}t\text{-}Bu)_4]$ (**C**) in the 400−2500 nm Range: Maximum Wavelength (nm) of Identified Absorption Bands, and Absolute Values (cm^{-1}) of the Double Exchange Parameters (B) and the Transfer Integrals ($\beta = 5B$) Estimated from the Optical Experiments

compound	400−800 nm	800−2500 nm	$\lvert B\rvert$[a]	$\lvert\beta\rvert$
1	435, 740	1320	758	3788
2	440, 730	1270	787	3937
4′	430, 725	1350	741	3704
5′	430, 710	1330	752	3759
6	435, 705	1340	746	3731
A	435, 660, 730	1390	719	3597
B	420, 545, 605, 650, 730	1360, 2050	735	3676
C	435, 570, 675, 760	1430, 2200	699	3497

[a] The NIR domain absorption band is located at energy $10|B|$.

the absorption spectra in the visible region, as well as inspection of the $\delta A(T)$ curves of these compounds (data not shown) while performing a careful comparison with the $\delta A(T)$ curves of the KBr matrix, allow identification of transitions whose maximum wavelengths are listed in Table 7, with also the positions of the absorption bands observed for **5′** and $(NEt_4)_2[Fe_4S_4(SCH_2C_6H_5)_4]$. All compounds possess, in addition to the intense charge transfer band at 420−440 nm, a band of weaker intensity, centered in the 700−760 nm range, which thus appears to be characteristic of the $[Fe_4X_4]^{2+}$ (X = S, Se) systems.

In the 800−2500 nm NIR region, a broad band centered around ∼1300 nm (Figure 11) is also a feature common to all spectra, including spectra of **5′** and $(NEt_4)_2[Fe_4S_4(SCH_2C_6H_5)_4]$ not shown. This band, lost in the tail of the absorption band of the visible region, is hardly detectable at room temperature. It becomes more intense and sharper with decreasing temperatures, as this is emphasized by the plot of the $\delta A(T)$ curves over the 800−2500 nm range (see insets). However, its intensity remains weak, and it cannot therefore be assigned to charge transfer transitions. The increase of its intensity and the decrease of its line width with decreasing temperatures can be accounted for by the variation of the thermal populations of the vibronic levels of the $|S_{12} = {}^9/_5, S_{34} = {}^9/_2, S, M_S; -\rangle$ ($S \in \{0, 1, 2\}$, $M_S \in \{-S, -S+1, ..., S\}$) electronic states, identified by our magnetization studies. Table 7 gives the maximum wavelength of this absorption band for all compounds, as deduced from the δA(300 K) curves.

Its location in the NIR energy range indicates that it can be assigned to the transitions associated with the electronic delocalization within the mixed-valence pairs. Indeed, according to the variable temperature MCD studies by Johnson et al.[51] of proteins containing valence-delocalized $S = {}^9/_2$ $[Fe_2S_2]^+$ units, such transitions are expected to occur in this NIR region. Estimates of the absolute values of the double exchange parameter B or of the transfer integral $\beta = 5B$ can directly be obtained from the energies at which these transitions are observed, using the relation $E_{opt} = 10|B| = 2|\beta|$. They are thus found to vary between 700 and 800 cm^{-1} (Table 7) and compare well with the $|B_{\Delta J=0}|$ of 600(100), 1000(100), and 1100(100) cm^{-1} obtained for compounds **3**, **4**, and **1**, respectively.

The similarity of features observed for the HiPIP models and the $(NEt_4)_2[Fe_4S_4(SCH_2C_6H_5)_4]$ and $(NEt_4)_2[Fe_4S_4(S\text{-}t\text{-}Bu)_4]$ compounds, as well as for the selenium-substituted $(NEt_4)_2[Fe_4Se_4(S\text{-}t\text{-}Bu)_4]$ compound, indicates that this band may well characterize the electronic delocalization within mixed-valence pairs not only of $[Fe_4S_4]^{2+}$-containing compounds but, more generally, of $[Fe_4X_4]^{2+}$ (X = S, Se) clusters. To our knowledge, this is the first report of the experimental observation of NIR electronic transitions associated with the electronic delocalization within mixed-valence $[Fe_4X_4]^{2+}$ (X = S, Se) model compounds.

Interestingly, in the case of the isomorph compounds $(NEt_4)_2[Fe_4S_4(S\text{-}t\text{-}Bu)_4]$ and $(NEt_4)_2[Fe_4Se_4(S\text{-}t\text{-}Bu)_4]$ which are structurally isomorph,[63] one notices that this NIR region band shows a slight shift toward lower energy by ∼360 cm^{-1} when one goes from $(NEt_4)_2[Fe_4S_4(S\text{-}t\text{-}Bu)_4]$ to $(NEt_4)_2[Fe_4Se_4(S\text{-}t\text{-}Bu)_4]$. In view of the fact that the Fe−Fe distances are longer in the selenium-substituted compound than in the nonsubstituted one (see Table 3), we tentatively attribute this shift mainly to the decrease of the Fe−Fe interaction within the mixed-valence pairs (decrease of the transfer integral β) accompanying the Fe−Fe distance lengthening. This shift thus may constitute further evidence of the assignment of this NIR electronic transition, present in all optically studied compounds, to Fe−Fe interactions within the mixed-valence pairs of $[Fe_4X_4]^{2+}$ (X = S, Se) clusters.

Spectra of $(NEt_4)_2[Fe_4S_4(S\text{-}t\text{-}Bu)_4]$ and $(NEt_4)_2[Fe_4Se_4(S\text{-}t\text{-}Bu)_4]$ (Figure 11) present a second band located at higher wavelengths: 2050 and 2200 nm, respectively. There is no clear evidence of the presence of this band in the other model compounds, and its origin remains to be elucidated. However, given the temperature dependence of the intensity and the line width of this band, as well as the shift toward lower energies by ∼330 cm^{-1} observed when going from $(NEt_4)_2[Fe_4S_4(S\text{-}t\text{-}Bu)_4]$ to $(NEt_4)_2[Fe_4Se_4(S\text{-}t\text{-}Bu)_4]$, it can tentatively also be assigned to Fe−Fe interactions.

Discussion

Redox Properties. HiPIPs are characterized by the existence and the stability of the $[Fe_4S_4]^{3+}$ core in their oxidized state. This appears to be promoted by the location of the cluster in a central hydrophobic pocket which prevents the hydrolysis of the oxidized core. This assumption was recently reinforced by the results of Agarwal et al.[12] who performed site-directed mutagenesis studies of the *C. vinosum* HiPIP; in particular, they demonstrated that, of the numerous aromatic residues (Tyr-19, His-42, Phe-48, Trp-60, Phe-66, Trp-76, and Trp-80) whose side chains are in the vicinity of the cluster, the residue Tyr-19 plays a major role in the protection of the oxidized core.

A $[Fe_4S_4]$ model compound must fulfill the previous condition of existence and stability of the $[Fe_4S_4]^{3+}$ core in order to be qualified as HiPIP relevant model. One working hypothesis to stabilize the oxidized core is to surround it with bulky thiolate ligands. The interest of such aromatic ligands was first evidenced by the use of the 2,4,6-

(73) Maes, E. M.; Knapp, M. J.; Czernuszewicz, R. S.; Hendrickson, D. N. *J. Phys. Chem. B* **2000**, *104*, 10878−10884.

triisopropylphenylthiolate ligand by Millar et al. to obtain and isolate the $\mathbf{1}^-$ complex.[15] The ligands we used for the $\mathbf{2}^{2-}$, $\mathbf{3}^{2-}$, $\mathbf{4}^{2-}$, $\mathbf{5}^{2-}$, and $\mathbf{6}^{2-}$ complexes are at least as bulky as the 2,4,6-triisopropylphenylthiolate ligand. Their protecting role is first illustrated by the fact that the electrochemical studies of these complexes show reversible or pseudoreversible $[Fe_4S_4]^{3+/2+}$ redox processes (Table 4). The $\mathbf{2}^-$, $\mathbf{5}^-$, and $\mathbf{6}^-$ anions are actually stable enough to be isolated as such in the solid state.[19,20] Thus, including the $\mathbf{1}^-$ anion,[15] there are now four isolated model compounds of the oxidized HiPIPs. Even though the $\mathbf{3}^-$ and $\mathbf{4}^-$ anions are not stable enough in solution to be isolated, we estimate that their ligands provide some degree of stabilization.

The difference in stability of the $\mathbf{1}^-$ and $\mathbf{4}^-$ anions is interesting as it confirms the importance of the protecting role played by the bulky aromatic ligands in the stabilization of the $[Fe_4S_4]^{3+}$ core. The change from $\mathbf{1}^{2-}$ to $\mathbf{4}^{2-}$ by addition of a CH_2 group corresponds to the bulky aromatic group 2,4,6-(*i*-Pr)$_3$C$_6$H$_2$ moving away from the $[Fe_4S_4]$ core, as indicated by the ^{1}H NMR properties of both compounds (decrease of the paramagnetic shifts and increase of the T_1 times, see Table 5). The increased distance of the 2,4,6-(*i*-Pr)$_3$C$_6$H$_2$ groups to the cluster in $\mathbf{4}^{2-}$ translates into the weakening of their protecting role and, consequently, into the decrease of the stability of the $[Fe_4S_4]^{3+}$ core. Another example illustrating the role played by the bulk of the aromatic ligands is given by the comparison of the redox properties of $\mathbf{4}^{2-}$ and $\mathbf{6}^{2-}$: the substituents of the ligand's phenyl ring are *t*-Bu groups instead of the *i*-Pr groups found in $\mathbf{4}^{2-}$, and the use of the more voluminous *t*-Bu substituents allows stabilization of the oxidized $\mathbf{6}^-$ species.

The same discussion can be transposed to the $\mathbf{2}^{2-}$ and $\mathbf{5}^{2-}$ anions, provided that one admits that only the phenyl substituents located at ortho and para positions play a role in the stabilization of the oxidized cluster. However, in the latter case, the phenyl rings are voluminous enough to avoid the decrease of the protecting role of the ligands' bulky part when one goes from $\mathbf{2}^{2-}$ to $\mathbf{5}^{2-}$.

A distinctive feature of $\mathbf{2}^{2-}$ and $\mathbf{5}^{2-}$ is that they do not exhibit the $[Fe_4S_4]^+$ reduced state. This redox peculiarity is shared with the HiPIPs. For both model compounds, the hypothesis we make is that the electronic density accompanying the phenyl rings located in the vicinity of the $[Fe_4S_4]$ cluster is such that the energy needed to bring another electron during the reduction is too high for the reduction to be observed.

Electronic Structure of $[Fe_4S_4]^{2+}$ Systems as Evidenced by Their Paramagnetism. 1. Reduced HiPIP from *C. vinosum*. High-quality magnetization data have been recorded on the reduced *C. vinosum* HiPIP over the rather wide 6−240 K temperature range. Their temperature dependence reflects the well-known antiferromagnetic behavior of this $[Fe_4S_4]^{2+}$ system. Fitting of the data within the exchange and double exchange theoretical framework has given satisfactory results. The positiveness of the values obtained for the exchange parameter *J*, in particular the positive *J* value of 282(2) cm^{-1} found for the best results (Table 1A), is consistent with the system's antiferromagnetic behavior. The value of the double exchange parameter *B* could not be determined from the fit of the magnetization data. However, optimal and close to optimal fit results are characterized by high (absolute) values of the effective $B_{\Delta J=0}$ parameter, $|B_{\Delta J=0}| \geq 800$ cm^{-1} (Table 1B), which account for the strong delocalization phenomenon occurring within the mixed-valence $[Fe_4S_4]^{2+}$ cluster. Actually, as discussed below, a $|B|$ value of 700−800 cm^{-1} can be deduced from the 77 K absorption spectrum reported by Cerdonio et al.[64]

Other authors have attempted to provide a quantitative description of the electronic structure of the reduced *C. vinosum* HiPIP based on the analysis of the temperature dependence of experimental data.[23,69] Antanaitis and Moss reported in 1975 the first magnetization studies of this protein,[23] and their report is the most recent one dealing with magnetization studies of this system. As the double exchange approach was not developed yet at that time for Fe−S systems, they relied on the pure Heisenberg approach to analyze their data. Using a single exchange parameter, they found a lower limit of 400 cm^{-1} for the average coupling constant. In our case, using the pure Heisenberg approach, the value of the average coupling constant which reads $(4J + 2(J + \Delta J))/6 = J + \Delta J/3$ turns out to be less than $J =$ 282(2) cm^{-1} as ΔJ takes negative values (Table 1A). It is clearly below the proposed limit of 400 cm^{-1}. This gap is not surprising since, with the exchange approach used by Antanaitis and Moss, all states sharing the same total electronic spin *S* are degenerated; it is then necessary to use important values for the unique exchange parameter to bring the degenerated paramagnetic levels sufficiently high in energy and thus moderate their contributions to the paramagnetic properties. Moreover, the Antanaitis and Moss measurements are subject to caution as they were performed with an analytical balance magnetometer and no paramagnetism could be detected for the reduced HiPIP up to 260 K. More recently, Bertini et al. studied the temperature dependence of the ^{1}H NMR isotropic shifts of the reduced HiPIP.[69] They demonstrated that the anti-Curie behavior of all signals could be accounted for either with an exchange approach or with an exchange and double exchange approach. They proposed values such as $J = 400$ cm^{-1} and $\Delta J = -200$ cm^{-1} for the former case, and values such as $J = 400$ cm^{-1} and $B = 400$ cm^{-1} for the latter case. However, no quantitative results concerning the electronic structure of the reduced HiPIP were reported, probably because of the small temperature range available by the NMR studies.

Consequently, it appears that our magnetization studies give, within the exchange and double exchange theoretical framework, a first reliable quantitative description of the electronic structure of the reduced *C. vinosum* HiPIP. This also includes the determination of its three lowest lying electronic levels $\mathcal{E}(S_{12} = {}^9/_2, S_{34} = {}^9/_2, S; --)$, $S \in \{0, 1, 2\}$. Their stabilization is due to an important gain of delocalization energy as attested by the strong ferromagnetic coupling observed within the mixed-valence pairs ($S_{ij} = {}^9/_2$, $(i, j) \in \{(1, 2), (3, 4)\}$). They remain the only thermally populated levels from cryogenic to ambient temperatures (Figure 5); they are therefore the only ones responsible for

the properties of the reduced HiPIP over this temperature range. The energy gaps between these three levels are governed by the exchange parameter J and simply follow the Landé rule.

2. HiPIP Relevant Synthetic Analogues. Six model compounds, four of which were newly synthesized, have also been the subject of our magnetization studies. The high-quality data obtained have been adjusted within the exchange and double exchange framework. The exchange parameter J takes positive values as expected for these antiferromagnetic systems, and, although the values of the double exchange parameter B could not be ascertained from the fit of the magnetization data, high $|B_{\Delta J=0}|$ values were found for the optimal and close to optimal fit results (Table 1B). $|B|$ values in the 700−800 cm^{-1} range could nevertheless be determined from variable temperature optical studies (Table 7). Here again, the gain of delocalization energy is responsible for the stabilization of the three lowest levels, $\mathcal{S}(S_{12} = {}^9/_2, S_{34} = {}^9/_2, S; --)$, $S \in \{0, 1, 2\}$; they alone are responsible for the systems' properties over the 0−300 K temperature range, as they remain the only ones populated in this temperature range. The energy gaps between these three levels also simply follow the Landé rule.

Holm et al.[24,25] have reported the magnetization studies of the $[Fe_4S_4]^{2+}$ models $(NEt_4)_2[Fe_4S_4(S-C_6H_5)_4]$ and $(NEt_4)_2[Fe_4S_4(S-CH_2-C_6H_5)_4]$. Their experimental curves, similar in shape to ours, indicate the depopulation of diamagnetic levels and the simultaneous population of paramagnetic levels in the 60−80 K temperature range. The interest of these compounds resides in the presence of phenylthiolate and benzylthiolate ligands which are not substituted, unlike the ones used in our case. Their data, however, were fitted in a pure exchange theoretical framework, making comparison between their results and ours meaningless.

The J values determined from the magnetization studies compare relatively well with the J value of 312 cm^{-1} recently proposed by Glaser et al.[21] to account for the superexchange contribution in $[Fe_4S_4]^{2+}$ systems, which they obtained by the use of S K-edge X-ray absorption spectroscopy to probe the covalency of Fe−S bonds and by exploiting the quadratic dependence they showed of the superexchange coupling constant on the covalency of Fe−μ-S bonds. However, unlike the B values found from the optical studies to be of the order of 700−800 cm^{-1}, they are spread over a large range of energy, from 261(2) cm^{-1} for compound **2** to 397(8) cm^{-1} for compound **3** (Table 1A). Such variations indicate that parameter J is likely to reflect the influence of the $[Fe_4S_4]^{2+}$ cluster's environment. We provide a working hypothesis below aimed at understanding such magnetostructural correlations in $[Fe_4S_4]^{2+}$ systems.

^{1}H NMR experiments additionally allowed us to probe the paramagnetism of the model compounds which is mainly due to the population of their first excited $\mathcal{S}({}^9/_2, {}^9/_2, 1; --)$ level but also, to a lesser extent, to the population of the second excited $\mathcal{S}({}^9/_2, {}^9/_2, 2; --)$ level (Figure 5B illustrates the population of these levels for the reduced HiPIP from *C. vinosum*). The observed very short T_1's mainly arise from a dipolar contribution. For complex $\mathbf{3}^{2-}$ and the highly biomimetic complexes $\mathbf{4}^{2-}$, $\mathbf{5}^{2-}$, and $\mathbf{6}^{2-}$, the paramagnetism also appears through the noticeable hyperfine shift of their SCH and SCH_2 protons (Table 5). In the case of the biomimetic complexes, the temperature dependence of the chemical shifts of their SCH_2 protons, recorded over the 245−330 K range (Figure 10A), follows an anti-Curie law similar to the one previously reported for the reduced HiPIP from *C. vinosum*[69] and other $[Fe_4S_4]^{2+}$ proteins.[70] We have simulated the paramagnetic contribution indicated by these temperature dependences using eq 9, the optimal values of J and B deduced from the adjustment of the magnetization data, and assuming a value of 1 MHz for the intrinsic site isotropic hyperfine coupling parameter A_0 (Figure 10B). The simulations indicate that the weight of the normalized paramagnetic shift contribution δ_p/A_0 decreases in the order $\mathbf{5}^{2-} > \mathbf{4}^{2-} > \mathbf{6}^{2-}$, which as expected is the inverse order of the J values (Table 1). These inequalities indeed reflect the rate at which the excited paramagnetic states become thermally populated for the different complexes. Comparison of the experimental and simulated curves then gives $A_0 =$ 3.6, 4.2, 2.7 MHz for complexes $\mathbf{4}^{2-}$, $\mathbf{5}^{2-}$, and $\mathbf{6}^{2-}$, respectively (Table 6). The $\delta_p(1/T)/A_0$ curve has also been calculated for the β-CH_2 protons of the cysteine ligands of *C. vinosum* (curves not shown), and, using the average value of the slopes of experimental $\delta_i(1/T)$ curves (which are segments with nearly identical slopes),[69] we have obtained for A_0 an average value of 4.2 MHz. Interestingly, calculated A_0 values compare well with the normalized isotropic coupling parameters obtained by ground state ^{1}H ENDOR studies of SCH_2 protons pertaining to ligands bound to mixed-valence pairs present in $[Fe_4S_4]^{3+}$ species generated by γ ray irradiation of $(N(C_2D_5)_4)_2[Fe_4S_4(SCH_2C_6D_5)_4]$ and $(N(C_2H_5)_4)_2[Fe_4S_4(SCH_2C_6H_5)_4]$ crystals (0.9−3.2 MHz),[74,75] and in the oxidized HiPIP from *Ectothiorhodospira halophila* iso-II[76] (0.6−3 MHz).

Two NIR Domain Absorption Bands as a Signature of $S = {}^9/_2$ Delocalized Mixed-Valence $[Fe_2X_2]^+$ (X = S, Se) Pairs. Variable temperature absorption spectroscopy studies have been performed on model compounds **1**, **2**, **4′**, **5′**, and **6**, as well as on $(NEt_4)_2[Fe_4S_4(SCH_2C_6H_5)_4]$, $(NEt_4)_2[Fe_4S_4(S-t-Bu)_4]$, and $(NEt_4)_2[Fe_4Se_4(S-t-Bu)_4]$, in the 400−2500 nm range and between 10 and 300 K. These optical studies permitted us to evidence for all compounds, in the NIR region, a broad absorption band which characterizes the complete electronic delocalization occurring within the $S_{ij} = {}^9/_2$ mixed-valence pairs ($(i, j) = \{(1, 2);(3, 4)\}$) of the clusters, and from which the magnitudes of the transfer integral β have been deduced to be in the 3500−3940 cm^{-1} range. For all studied $[Fe_4X_4]^{2+}$ (X = S, Se) models compounds, the striking similitude observed between the position, width, and temperature dependence of this band indicates that the Fe−Fe interactions responsible for the

(74) Mouesca, J.-M.; Rius, G.; Lamotte, B. *J. Am. Chem. Soc.* **1993**, *115*, 4714−4731.
(75) Noodleman, L.; Chen, J.-L.; Case, D. A.; Giori, C.; Rius, G.; Mouesca, J.-M.; Lamotte, B. *Nucl. Magn. Reson. Paramagn. Macromol.* **1995**, 339−367.
(76) Kappl, R.; Ciurli, S.; Luchinat, C.; Hüttermann, J. *J. Am. Chem. Soc.* **1999**, *121*, 1925−193.

electronic delocalization (quantified by β) do not change spectacularly among the studied systems. This statement is actually in agreement with the admitted conjecture, deduced from the comparison between known structures of the $[Fe_4X_4]^{2+}$ (X = S, Se) system, that the core geometry is likely to be conserved in all such systems, especially the Fe−Fe distances ruling the direct interactions between the iron sites.

The width of this NIR domain absorption band indicates an important Huang−Rhys factor. For the electronic states involved in this electronic transition, the differences in the geometries of the $[Fe_4X_4]^{2+}$ (X = S, Se) systems, which are reflected in the band's width, can be explained by the bonding and antibonding characters of the molecular orbitals involved in this one-electron transition and, consequently, by significant differences in the vibronic coupling forces present in both states. Moreover, due to such differences in geometries, small Franck−Condon factors may be associated with the vibronic components of this transition, and they may be responsible to a great extent for the weak intensity of this transition.

It should be noted that, concerning $[Fe_4X_4]^{2+}$ (X= S, Se) clusters, the observation of an absorption band in the NIR region was so far only reported once, in 1974, by Cerdonio et al., for the reduced *C. vinosum* HiPIP.[64] The 77 K spectrum of the reduced protein indeed reveals a broad band at 9615 cm^{-1} (1040 nm), which was tentatively assigned to either an intracluster transition between inequivalent Fe sites or one or more d−d transitions. The latter possibility was discarded by the authors on the argument that Mössbauer data rule against the presence of a localized Fe(II) subunit in the reduced HiPIP.[64,77] In agreement with this, we associate this transition with the electronic delocalization occurring within the mixed-valence pairs of the $[Fe_4S_4]^{2+}$ core. This transition appears therefore as the blue-shifted counterpart of the one observed for the models. Assuming as previously that this transition energy corresponds to $10|B|$, one obtains for the protein a $|B|$ value of 962 cm^{-1} ($|\beta| = 4810$ cm^{-1}). However, considering the narrow range spanned by the $|B|$ values as deduced from the optical studies of several chemically different $[Fe_4X_4]^{2+}$ (X = S, Se) analogues (Table 7), we believe that the noticeable blue shift of this transition reflects differences in the local structures of the Fe sites in the protein, rather than an increase of the magnitude of the transfer integral β (or equivalently B). Indeed, when one takes into account the difference Δ between the zero order energies of the two configurations originating from the possible locations of the excess electron on one of the Fe sites of a mixed-valence pairs, the energy of such a transition becomes[53] $\sqrt{\Delta^2+B^2(2S_{ij}+1)^2} \geq |B|(2S_{ij}+1)$, with $S_{ij} = {}^9/_2$ in our case. Given that $|\Delta|$ is expected to be far more important in proteins than in the models where the environment of the Fe ions is chemically equivalent, the observed blue shift is more likely indicative of differences in the valence-delocalized character of the studied systems. Finally, using $|B|$ values in the 700−800 cm^{-1} range given by the optical studies of the models (Tab 7), we predict for the reduced HiPIP trapping energy differences Δ in the 5300−6600 cm^{-1} range.

Recently, the electronic properties of proteins containing a valence-delocalized $S = {}^9/_2$ $[Fe_2S_2]^+$ unit (namely, the reduced $[Fe_2S_2]^+$ ferredoxin from *Clostridium pasteurianum* in high-pH media and in its mutated C56S and C60S forms, and proteins containing $[Fe_3S_4]^0$, $[ZnFe_3S4]^+$, and $[Fe_4S_4]^+$ cores) have been investigated by Johnson et al.[51] Taking advantage of the paramagnetic nature of the ground states of these proteins, the authors used MCD spectroscopy to evidence a pattern of three MCD absorption bands which proves to be characteristic of the presence of valence-delocalized $S = {}^9/_2$ $[Fe_2S_2]^+$ units. The three absorption bands correspond to one-electron transitions from a doubly occupied $\sigma(+)$ orbital toward unoccupied $\sigma(-)$, $\pi(+)$, $\pi(-)$ orbitals, where the bonding and antibonding $\sigma(\pm)$ (respectively $\pi(\pm)$) orbitals result from the σ (respectively π) interactions of orbitals of mainly d_{z^2} (respectively d_{xz}, d_{yz}) character. They directly deduced from the electric-dipole-allowed $\sigma(+) \rightarrow \sigma(-)$ transition, absolute values of the transfer integral which are in the 3950−4650 cm^{-1} range and comparable to the values we report for the $[Fe_4X_4]^{2+}$ (X = S, Se) systems (3500−3940 cm^{-1}). It is, however, likely that their reported $|\beta|$ values of 3950−4650 cm^{-1} need to be corrected from trapping energy contributions as this was done above for the reduced HiPIP. The 3500−4650 cm^{-1} range spanned by the experimental $|\beta|$ values remains nevertheless narrow, indicating that the σ-delocalization pathway seems to be remarkably conserved within the mixed-valence $[Fe_2S_2]^+$ pairs of all the investigated $[Fe_2S_2]^+$, $[Fe_3S_4]^0$, $[ZnFe_3S4]^+$, $[Fe_4S_4]^+$, or $[Fe_4X_4]^{2+}$ (X = S, Se) clusters.[78] The $\sigma(+) \rightarrow \pi(+)$ transition gives rise in the MCD spectra to shoulders at wavelength values greater than 800 nm and is electric-dipole forbidden, contrarily to the $\sigma(+) \rightarrow \pi(-)$ transition which is electric-dipole allowed and is located approximately in the 600−700 nm range. It is interesting to note that the spectra of $(NEt_4)_2[Fe_4S_4(SCH_2C_6H_5)_4]$, $(NEt_4)_2[Fe_4S_4(S\text{-}t\text{-}Bu)_4]$, and $(NEt_4)_2[Fe_4Se_4(S\text{-}t\text{-}Bu)_4]$ all present an absorption band at ~660 nm (Table 7), and that, similarly, the 77 K absorption spectrum of the reduced *C. vinosum* HiPIP also exhibits a marked shoulder at ~600 nm.[64] We believe that these absorption bands can

(77) In the case of the transitions we have observed, we also discard the possibility of d−d transitions for similar reasons. Mössbauer studies of the HiPIP models performed at 77 K indicate no valence trapping (results will be published elsewhere).

(78) The relatively narrow range obtained for $|\beta|$ from experimental one-electron transition energies ($\beta \approx 3500-4650$ cm^{-1}) raises the question of the reliability of the theoretical determination of β since theoretical values of 1000−7750 cm^{-1} are reported in the literature.[21,44,63] Such a comparatively very large variation illustrates the difficulty of the theoretical determination of β. For instance, the quantity β can be obtained from density functional theory (DFT) calculations as the differences of the Kohn−Sham (KS) orbital energies which, resulting from the bonding and antibonding linear combinations of the d-orbitals, represent the σ-delocalization pathway. Proceeding this way, very distant β values of ~4250 and ~7750 cm^{-1} have been predicted for $[Fe_2S_2]^+$ and $[Fe_4S_4]^{2+}$ clusters (see refs 21, 82, and references therein). In fact, although KS eigenvalue differences correspond to zero order excitation energies and, as such, can actually give very good estimates of these excitation energies, the use of this approach needs careful consideration as most currently used DFT implementations fail to give accurate KS eigenvalues because of the wrong asymptotic behaviors of popular LDA and GGA exchange-correlation potentials.[83−86]

be considered as the counterpart in these $[Fe_4X_4]^{2+}$ systems of the $\sigma(+) \rightarrow \pi(-)$ transition observed by MCD spectroscopy. No clear evidence of such an absorption band in the 600−700 nm range could nevertheless be found in the variable temperature spectra of the other HiPIP models. In addition to these three MCD bands, a fourth band is observed in the 700−800 nm range, which has been shown by Johnson et al.[51] to be also characteristic of valence-delocalized $S = {}^9/_2$ $[Fe_2S_2]^+$ unit. We note that the absorption spectra of all studied model compounds also possess the analogue of this MCD band (Table 7) in this wavelength range. Moreover, a similar band is present at 700 nm in the 77 K absorption spectrum of the reduced *C. vinosum* HiPIP.[64] It therefore appears that the two absorption bands we have observed in the 700−1500 nm NIR region are a hallmark of the presence not only of valence-delocalized $S = {}^9/_2$ $[Fe_2S_2]^+$ unit but more generally of valence-delocalized $S = {}^9/_2$ $[Fe_2X_2]^+$ (S = S, Se) clusters.

Estimates of the ΔJ Parameter. Two parameters were initially proposed for describing exchange interactions in the investigated $[Fe_4S_4]^{2+}$ systems: J, the coupling constant linking $Fe^{2.5+}$ sites pertaining to different pairs; and ΔJ which helps define the coupling constant within the mixed-valence pairs by the relation $J + \Delta J$. Because of the compression of the $[Fe_4S_4]^{2+}$ core along the S_4 axis, the Fe−S distances between the mixed-valence pairs are shorter than the Fe−S distances in the mixed-valence pairs, leading to a stronger superexchange interaction between the pairs than in the pairs. ΔJ is thus expected to take negative values and also to give a measure of the distortion of the core.[21,63] Clearly, its relevance to a correct description of the electronic structure of $[Fe_4S_4]^{2+}$ systems is indubitable. However, the covariance between B and ΔJ ruled out the possibility to simultaneously determine both parameters from the fit of the magnetization data. ΔJ was thus set to zero, and, for the probe temperature range used, the results of the magnetization studies evidenced that a single coupling constant suffices to account for the exchange interaction contributions to the gaps between the ground and lowest lying electronic levels of the $[Fe_4S_4]^{2+}$ clusters, the double exchange contributions being then accounted for by $B_{\Delta J=0}(S_{ij} + {}^1/_2)$ terms. As shown by Crozet et al., the effective double exchange parameter $B_{\Delta J=0}$ is actually related to B through[63]

$$B_{\Delta J=0} = B - \frac{9}{2}\Delta J$$

with $B > 0$ and $\Delta J \leq 0$. Since B was found by optical studies to be of 700−800 cm^{-1}, the above relation allows us to deduce ΔJ from the knowledge of $B_{\Delta J=0}$. However, among the studied clusters, this is only possible in the case of compounds **1**, **3**, and **4** for which the value of $B_{\Delta J=0}$ could be determined (Table 1A). Thus, given the uncertainties in the $B_{\Delta J=0}$ and B values (and with ΔJ constrained to take negative values), we obtain that ΔJ vanishes for **3** and that it lies between −89 and −66 cm^{-1} for **1**, and between −66 and −44 cm^{-1} for **4**. In the case of the reduced HiPIP and the other model compounds, there only is for ΔJ the lower limit of $-J$ (Table 1A) which is due to the fact that the exchange coupling within the mixed-valence pairs is expected to be antiferromagnetic ($J + \Delta J \geq 0$). According to us, the values taken by ΔJ in these compounds must be very negative leading to $B_{\Delta J=0}$ deviating significantly from the $|B|$ values of 700−800 cm^{-1} (because of the $(-9/2)\Delta J$ contribution to $B_{\Delta J=0}$), and thus to $B_{\Delta J=0}$ not being accessible experimentally despite the large temperature range used.

With the three complexes, **1**, **3**, and **4**, for which both J and ΔJ could be estimated, we achieve to our knowledge the first experimental quantitative characterization of heterogeneous exchange interactions in $[Fe_4S_4]^{2+}$ systems. Interestingly the $|\Delta J|/J$ ratios calculated using the ΔJ estimates suggest that the distortion of the $[Fe_4S_4]^{2+}$ core increases in the order $3 \ll 4 \leq 1$. Magnetostructural correlations are thoroughly discussed below using considerations based on the J parameter which offers the advantage that its value is available for all studied $[Fe_4S_4]^{2+}$ compounds.

Magnetostructural Correlations in $[Fe_4S_4]^{2+}$ Systems. The results of our magnetic and optical studies suggest that, up to room temperatures, $[Fe_4X_4]^{2+}$ (X = S, Se) systems may be viewed as resulting from the antiferromagnetic coupling between two valence-delocalized $S_{ij} = {}^9/_2$ $[Fe_2X_2]^+$ (X = S, Se) units. The strength of the antiferromagnetic coupling is quantified by the J parameter, which proves to be sensitive to the change in the chemical environment of the core. There is, however, no simple relationship between the values taken by J and ligands' structural features such as, for example, the biomimetic character of the thiolate ligands (presence of a SCH or SCH_2 group). Thus, J values close to the one determined for the reduced HiPIP are obtained for compound **2** and also for the more biomimetic compound **5** (Table 1).

Nevertheless, the model compounds can be divided into three sets, $\mathcal{J}_0$, $\mathcal{J}_+$ and $\mathcal{J}_-$, on the basis of their J values: set $\mathcal{J}_-$ contains compounds **2** and **5** whose J values are closest to the one found for the reduced *C. vinosum* HiPIP, whereas set $\mathcal{J}_0$ (respectively $\mathcal{J}_+$) holds compounds **1**, **4**, and **6** (respectively compound **3**) with higher J values (respectively the highest J value). When one then considers the bulk of the complexes' ligands, it appears that the membership to the different sets is correlated with the bulk of the involved ligand: $\mathcal{J}_+$ (respectively $\mathcal{J}_-$) holds the compound with the less bulky (respectively bulkiest) ligands, and ligands of compounds in $\mathcal{J}_0$ are of intermediate bulk. We thus draw for $[Fe_4S_4]^{2+}$ model compounds the following trend: the bulkier the ligands, the lower the J value taken among what actually is a continuum of available positive values. A further evidence of this trend is given by recent results of ^{13}C NMR studies of compounds $(NEt_4)_2[Fe_4S_4(SCH_2C_6H_5)_4]$ and $(NEt_4)_2$-$[Fe_4S_4(S\text{-}t\text{-}Bu)_4]$:[63] analysis of the temperature dependence of the data, performed within the exchange and double exchange framework, gives J values of 433 and 383 cm^{-1}, respectively. Thus both compounds belong to the $\mathcal{J}_+$ set, and the fact that their ligands are of small bulk agrees with the observed trend. We note in passing that the same trend apparently can be drawn from the coupling parameter ΔJ since the $-\Delta J$ values of ∼0, 44−66, and 66−89 cm^{-1} estimated for the complexes **3**, **4**, and **1**, respectively, increase

with the bulk of the ligands. This enforces the assumption made above that ΔJ must be far more negative for the other complexes since the ligands of these latter ones are bulkier.

Such a trend has its physical origin in the fact (i) that the antiferromagnetic coupling is mediated by the Fe−μ_3-S−Fe superexchange pathways and (ii) that, consequently, the strength of the overall antiferromagnetic coupling quantified by J gives a measure of the distortions of the $[Fe_4S_4]^{2+}$ core due to the outer chemical environment. From a magneto-structural point of view, these distortions correspond to a more or less pronounced deviation of the core's geometry from an ideal geometry wherein the efficiency of the coupling pathway is optimum. The necessarily theoretical determination of this ideal geometry is beyond the scope of the present study. However, we guess it should be the Jahn−Teller D_{2d} distorted geometry of the isolated $[Fe_4S_4]^{2+}$ cluster,[44] of which known crystal structures seem to be reminiscent. This hypothesis appears to be supported by the fact that the $[Fe_4S_4]$ cubanes of compounds $(NEt_4)_2[Fe_4S_4(S\text{-}t\text{-}Bu)_4]$ and $(NEt_4)_2[Fe_4S_4(SCH_2C_6H_5)_4]$, which are in the $\mathcal{J}_+$ set, have respectively real and nearly D_{2d} symmetries,[47,79] whereas there are noticeable deviations from D_{2d} in the case of compound **2**, which is in the $\mathcal{J}_-$ set.

When one considers the mean terminal Fe−S bond lengths given in Table 3 for $[Fe_4S_4]^{2+}$ systems, it tends to increase with the bulk of the cavity occupied by the cluster, the cavity being constituted either by the ligands in the models or by the residues' side chains near the cluster in the proteins, the conformations of which determine the cavity's shape (in the case of the reduced HiPIP, the bulk is tied to the presence of numerous aromatic residues' side chains in the vicinity of the cluster). Moreover, considering the systems whose J constants have been reported, one notes that the mean distance decreases in the order $\mathbf{2}^{2-}$, 2.287 Å > reduced HiPIP, 2.272 Å > $[Fe_4S_4(S\text{-}t\text{-}Bu)_4]^{2-}$, 2.254 Å > $[Fe_4S_4(SCH_2C_6H_5)_4]^{2-}$, 2.251 Å, which is found to be the reverse order of the J values (261(2), 282(2), 383, and 433 cm^{-1}, respectively; values from this work (Table 1A) and ref 63). It therefore appears that the influence of the outer chemical environment on the cluster's geometry can be explained by the control it exerts over the volume which is made available to the cluster within the cavity. This control is related to the bulk of the constituents which defines, for sterical reasons, the extent to which the cavity can contract and bring the constituents close to the cluster and to each other. The cavity's size then intervenes in determining the cluster's geometry and the efficiency of the superexchange pathways, through the fact that the final geometry should maximize the bonding Fe−S(ligand) interactions; that is, with the Fe−S(ligand) interactions acting as the driving force, the cluster undergoes an expansion and concomitant distortions which are all the more important as the terminal ligands are located further apart from the cluster, that is, as the cavity is large. Hence, we propose that the antiferromagnetic coupling in $[Fe_4S_4]^{2+}$systems is probably primarily controlled by the tightness of the cluster's fit within the cavity provided by its environment. Recalling the resemblance pointed out by Silver et al.[80] between conformational effects in protein and compression effects, it is convenient to establish here an analogy between the influence of the cluster's environment and a "chemical pressure" effect due to the more or less tight fit of the cluster within its cavity. This pressure has to be counted negatively, as it tends to dislocate the cluster, and its magnitude decreases with the tightness of the fit within the cavity.

Table 8. Composition of the $\mathcal{J}_{0,\pm}$ Sets[a]

J_-	**2**	**5**
J (cm^{-1})	261(2)	312(2)
$-\Delta J$ (cm^{-1})		
$[Fe_4S_4]^{3+/2+}$	yes[b]	yes[b]
$[Fe_4S_4]^{2+/+}$	no	no

J_0	**1**	**4**	**6**
J (cm^{-1})	320(3)	331(2)	362(2)
$-\Delta J$ (cm^{-1})	66−89	44−66	
$[Fe_4S_4]^{3+/2+}$	yes[b,c]	yes	yes[b]
$[Fe_4S_4]^{2+/+}$	yes[c]	yes	yes

J_+	[A][d]	**3**	[B][e]
J (cm^{-1})	383[d]	397(8)	433[e]
$-\Delta J$ (cm^{-1})		∼0	
$[Fe_4S_4]^{3+/2+}$	yes[f]	yes	yes[f]
$[Fe_4S_4]^{2+/+}$	yes[f]	yes	yes[f]

[a] For each compound, the J value (Table 1A), the estimated ΔJ value (if available) and the observed redox couples are indicated; the fact that the oxidized species have been isolated is also indicated. One can refer to Table 4 and ref 88 for the $E_{1/2}$ values and the reversible character of the redox processes. [b] $[Fe_4S_4]^{3+}$ species isolated in the solid state. [c] Reference 15. [d] [A] ≡ $(NEt_4)_2[Fe_4S_4(S\text{-}t\text{-}Bu)_4]$.[63] [e] [B] ≡ $(NEt_4)_2[Fe_4S_4(SCH_2C_6H_5)_4]$.[63] [f] Reference 88.

Finally, it seems to us that the magnetostructural correlations in $[Fe_4S_4]^{2+}$ systems especially deserve further studies. Thus, from an experimental viewpoint, the dependence of the J parameter upon the external pressure should be investigated, and we expect J to be increasing as a function of the external pressure, since it should tend to compensate the chemical pressure effect. In parallel, theoretical models should be devised which allow one to account for the influence of the outer coordination sphere on the magnetic properties. In this respect, we believe that a vibronic model is likely to give an insight of the involved mechanism by integrating the coupling between the bridging and terminal Fe−S vibrational modes which have been identified by RR spectroscopy for a couple of $[Fe_4S_4]^{2+}$ analogues.[73]

$[Fe_4S_4(SCH_2\text{-}2,4,6\text{-}(Ph)_3C_6H_2)_4]^{2-}$ Complex as the Best Model of the Reduced HiPIPs. In order to compare the relevance of the different reduced HiPIP models, we have put together in Table 8 the composition of the $\mathcal{J}_{0,\pm}$ sets and the observed redox behavior of their components. Complex $\mathbf{5}^{2-}$ can thus be considered as the best model reported so far for the reduced HiPIPs: (i) as the HiPIP, it does not exhibit the $[Fe_4S_4]^{+}$ redox state while its oxidized $[Fe_4S_4]^{3+}$ form is stable enough to be isolated in the solid state;[19] (ii) its ligands have the SCH_2 group present in cysteine; (iii) its overall

(79) Averill, B. A.; Herskovitz, T.; Holm, R. H.; Ibers, J. A. *J. Am. Chem. Soc.* **1973**, *95*, 3523−3534.

(80) Silver, J.; Fern, G. R.; Miller, J. R.; McCammon, C. A.; Evans, D. J.; Leigh, G. J. *Inorg. Chem.* **1999**, *38*, 4256−4261.

magnetic behavior compares well with that of the reduced HiPIP from *C. vinosum*.

Conclusion

The electronic structures of the reduced *C. vinosum* HiPIP and the relevant model complexes $\mathbf{1}^{2-}$, $\mathbf{2}^{2-}$, $\mathbf{3}^{2-}$, $\mathbf{4}^{2-}$, $\mathbf{5}^{2-}$, and $\mathbf{6}^{2-}$ have been characterized using variable temperature magnetization and optical measurements. The main results and conclusions obtained during these studies are summarized below.

(1) The electrochemical characterization of the newly synthesized $\mathbf{2}^{2-}$, $\mathbf{3}^{2-}$, $\mathbf{5}^{2-}$, and $\mathbf{6}^{2-}$ complexes confirms that the presence of bulky ligands allows, as in the case of complexes $\mathbf{1}^{2-}$ and $\mathbf{4}^{2-}$, the stabilization the $[Fe_4S_4]^{3+}$ oxidation state. Differences in the stability of studied solvated $[Fe_4S_4]^{3+}$ species then arise from differences in the protection against solvolysis offered by the ligands. For $\mathbf{2}^{2-}$ and $\mathbf{5}^{2-}$, the presence of numerous phenyl rings probably makes the $[Fe_4S_4]^{+}$ redox state electrochemically unavailable by making prohibitive the electrical work required to bring an additional electron. The difficult observation of this redox state in HiPIPs could also be explained by the important presence of aromatic rings in the vicinity of the cluster.

(2) The X-ray structure of the novel $\mathbf{2}^{2-}$ complex has been solved. It reveals a $[Fe_4S_4]$ core which is remarkably capped by the ligands' phenyl rings, and whose compressed D_{2d}-distorted geometry is similar to those reported so far for $[Fe_4S_4]^{2+}$ model compounds and proteins.

(3) From the analysis of the magnetization data within the exchange and double exchange theoretical framework, we have determined a reliable quantitative description of the electronic structure of the reduced HiPIP and the relevant model compounds. They may be viewed, up to room temperatures, as resulting from the antiferromagnetic coupling between two valence-delocalized and ferromagnetically coupled $[Fe_2S_2]^{+}$ units, wherein the ferromagnetic coupling is strongly promoted by the spin-dependent electronic delocalization phenomenon. Within the available large temperature range, the electronic properties of the studied systems can be accounted for by population of the electronic levels $\mathcal{E}(S_{12} = {}^9/_2, S_{34} = {}^9/_2, S; --)$, $S \in \{0, 1, 2\}$, the excited paramagnetic triplet and quintet levels lying respectively J and $3J$ above the diamagnetic ground level. This description of the systems' electronic structure has permitted the analysis of the temperature dependence of the chemical shifts of SCH_2 protons pertaining to the coordinating cysteines of the HiPIP and to the ligands of the biomimetic complexes $\mathbf{4}^{2-}$, $\mathbf{5}^{2-}$, $\mathbf{6}^{2-}$, and the determination of their hyperfine coupling constants in the 2.7−4.2 MHz range.

(4) The range spanned by the J values (261−397 cm^{-1}) reflects differences in the geometry of the $[Fe_4S_4]^{2+}$ core which are due to the different outer chemical environments. Although known structures of $[Fe_4S_4]^{2+}$ synthetic analogues and proteins show no drastic geometry changes, it thus appears that the observed small changes are critical from a magnetostructural point of view. Considering the bulk of the ligands used for the HiPIP models, we draw the trend that J decreases with increasing bulk. Moreover, we note that the terminal Fe−S bond length tends to increase with the bulk of the cavity occupied by the cluster. From both observations, antiferromagnetic coupling in $[Fe_4S_4]^{2+}$ systems seems to be essentially controlled by the more or less tight fit of the cluster within the cavity where it is located. This hypothesis deserves of course further studies.

(5) Variable temperature optical studies have been performed on the reduced HiPIP relevant models, as well as on the $(NEt_4)_2[Fe_4S_4(SCH_2C_6H_5)_4]$ compounds and the isomorph $(NEt_4)_2[Fe_4S_4(S\text{-}t\text{-}Bu)_4]$ and $(NEt_4)_2[Fe_4Se_4(S\text{-}t\text{-}Bu)_4]$ analogues. All spectra present two absorption bands centered in the 705−760 and 1270−1430 nm ranges, which have been identified as a hallmark of the presence of valence-delocalized and ferromagnetically coupled $[Fe_2X_2]^{+}$ (X = S, Se) units. From the position of the latter band, one directly determines $|B|$ values of 699−787 cm^{-1} (or, equivalently, $|\beta|$ values of 3497−3937 cm^{-1}). Both bands are also present at 700 and 1040 nm in the 77 K spectrum of the reduced HiPIP from *C. vinosum*.[64] The origin of the blue shift observed for the low-energy band has been ascribed to the inequivalent environments of the iron sites in the protein, rather than to an increase of $|\beta|$, because of the similarity observed in the structures of $[Fe_4S_4]^{2+}$ clusters, especially in the Fe−Fe distances upon which β depends.

(6) For compounds **3**, **4**, and **1**, the results of the magnetization and optical studies have allowed a complete characterization of the exchange interaction within the $[Fe_4S_4]^{2+}$ clusters given by respective J values of ≈397, ≈331, and ≈320 cm^{-1} and $-\Delta J$ estimates of ∼0, 44−66 and 66−89 cm^{-1}.

(7) The highly biomimetic complex $[Fe_4S_4(SCH_2\text{-}2,4,6\text{-}(Ph)_3C_6H_2)_4]^{2-}$ appears to be the best model reported so far for the reduced HiPIPs from the point of view of its redox and overall magnetic properties.

Acknowledgment. We are indebted to Jean-Marc Moulis for the gift of the high-quality protein sample, Gérard Desfonds for his valuable help in setting up the optical experiment, and Maria Parobets-Desfonds and Fabrice Moriaud for providing high-quality samples of $(NEt_4)_2[Fe_4Se_4(S\text{-}t\text{-}Bu)_4]$ (M.P.-D.) and $(NEt_4)_2[Fe_4S_4(SCH_2C_6H_5)_4]$ and $(NEt_4)_2[Fe_4S_4(S\text{-}t\text{-}Bu)_4]$ (F.M.). We express our gratitude to Catherine Bougault for very helpful comments.

Supporting Information Available: Control isotherm absorption spectra of KBr in the visible and NIR domains (Figure S1). Error map obtained by fitting the susceptibility data of the reduced HiPIP with a pure exchange approach (Figure S2). The plot against B of the n' and TIC_H parameter values obtained by fitting the magnetization data of the reduced HiPIP (Figure S3) within the exchange and double exchange theoretical framework. ORTEP[81] view of the $[Fe_4S_4(SC)_4]$ unit of $[Fe_4S_4(S\text{-}2,6\text{-}(Ph)_2C_6H_3)_4]^{2-}$

(81) Farrugia, L. J. *J. Appl. Crystallogr.* **1997**, *30*, 565 (Ortep 3 for Windows).

showing the 50% probability ellipsoids, principal atomic distances, and the atom-labeling scheme (Figure S4). The plot against B of the n', D, and TIC_H parameter values obtained by fitting the magnetization data of the model compounds within the exchange and double exchange theoretical framework (Figure S5). Crystallographic data (excluding structure factors) for the reported structure as a crystallographic information file. This material is available free of charge via the Internet at http://pubs.acs.org.

IC034494N

(82) Li, J.; Nelson, M. R.; Peng, C. Y.; Bashford, D.; Noodleman, L. *J. Phys. Chem. A* **1998**, *102*, 6311−6324.
(83) Casida, M. E.; Casida, K. C.; R., S. D. *Int. J. Quantum Chem.* **1998**, *70*, 933−941.
(84) Savin, A.; Umrigar, C. J.; Gonze, X. *Chem. Phys. Lett.* **1998**, *288*, 391−395.
(85) Grüning, M.; Gritsenko, O. V.; van Gisbergen, S. J. A.; Baerends, E. J. *J. Chem. Phys.* **2001**, *114*, 652−660.
(86) Casida, M. E. In *Accurate description of low-lying molecular states and potential energy surfaces*; ACS Symposium Series 828; Hoffmann, M. R., Dyall, K. G., Eds.; American Chemical Society: Washington, DC, 2002 (Proceedings of ACS Symposium, San Diego, CA, 2001); pp 199−220.
(87) Parisini, E.; Capozzi, F.; Lubini, P.; Lamzin, V.; Luchinat, C.; Sheldrick, M. *Acta Crystallogr.* **1999**, *D55*, 1773−1784.
(88) Blonk, H. L.; Kievit, O.; Roth, E. K.-H.; Jordanov, J.; van der Linden, J. G. M.; Steggerda, J. J. *Inorg. Chem.* **1991**, *30*, 3231−3234.